# Elastic limit tensile stress of UHPFRC: Method of determination and effect of fiber orientation

Jian Zhan [*], Emmanuel Denarié, Eugen Brühwiler

*Laboratory of Maintenance and Safety of Structures (MCS), Swiss Federal Institute of Technology Lausanne (EPFL), Lausanne, Switzerland*

## ARTICLE INFO

## ABSTRACT

This paper discusses the influence of fiber orientation on elastic limit tensile stress of ultra-high performance fiber reinforced cementitious composites (UHPFRC). An original model relating elastic limit tensile stress to fiber orientation is proposed, and three determination methods of the elastic limit are compared. Five specimens are tested under uniaxial tension and characterized with digital image correlation, acoustic emission and displacement transducers. Before testing, the fiber distribution (local dosage and orientation) of each specimen is determined using a magnetic probe. After testing, three methods (offset with 2 different threshold values, and deformation modulus drop) are applied to determine the elastic limit tensile stress. The test results show that the proposed model estimates well the elastic limit tensile stress on the basis of fiber orientation. The modulus-drop method yields the most representative value for the elastic limit considering the underlying physical phenomena. It may be taken as definition of elastic limit tensile stress of UHPFRC.

## 1. Introduction

Ultra-high Performance Fiber Reinforced Cementitious Composites (UHPFRC) present remarkable mechanical properties and a dense matrix. A commonly accepted definition of UHPFRC in terms of material properties is: (1) average elastic limit tensile stress larger than 7 MPa, (2) average tensile strength from 8 to 14 MPa, (3) strain hardening deformation from 1 to 5‰, (4) 5%-fractile characteristic value of compressive strength larger than 120 MPa. Design of UHPFRC members with strain hardening mixes enables a waterproof and crack-free material at serviceability, thus providing protection against water and chloride ion ingress [1–3].

The uniaxial tensile response of strain-hardening UHPFRC can be divided into three main domains, i.e., elastic domain, strain-hardening domain and softening domain [4,5]. As shown in Fig. 1 for a strain hardening response, the elastic limit tensile stress $f_{Ute}$, hereafter called elastic limit, is higher than the matrix tensile strength $\sigma_{mu}$ and lies at the transition region from elastic behavior to the strain-hardening or softening behavior. It is also called first cracking strength [5,6] or limit of elasticity under tension [7].

Starting from the matrix tensile strength, matrix discontinuities (micro-cracks invisible to naked eye) progressively develop inside the material followed by a single localized macro-crack beyond the tensile

strength [4]. Consequently, material properties of UHPFRC degrade beyond the elastic domain, e.g., deformation modulus decreases and permeability increases, progressively impairing properties relevant for serviceability of structures. Besides, the elastic limit is a relevant parameter to characterize the fatigue stress level and is directly involved in the fatigue design of UHPFRC structures [8,9].

In order to improve knowledge of UHPFRC material behavior, it is important to have an objective and practical method for the determination of the elastic limit. However, knowledge on the mechanisms governing the elastic limit of UHPFRC is scarce and the objective determination of the elastic limit remains challenging.

Literature shows that the elastic limit not only is a function of matrix properties, but also is strongly affected by the orientation, volume, type and geometry of fibers. Tjipobroto [10,11] first highlighted the potential of high fiber dosage to increase the elastic limit of fiber-reinforced concrete (FRC) containing different volume fractions (0–12%) of discontinuous fibers. Wille et al. [5] and Delsol et al. [12] confirmed a similar trend for UHPFRC. However, high fiber dosage does not necessarily lead to high elastic limit, as bond, orientation and other parameters of fibers also matter [13]. With very detrimental fiber orientation, fibers even may act as defects and can lead to elastic limits much lower than the plain matrix tensile strength [14,15].

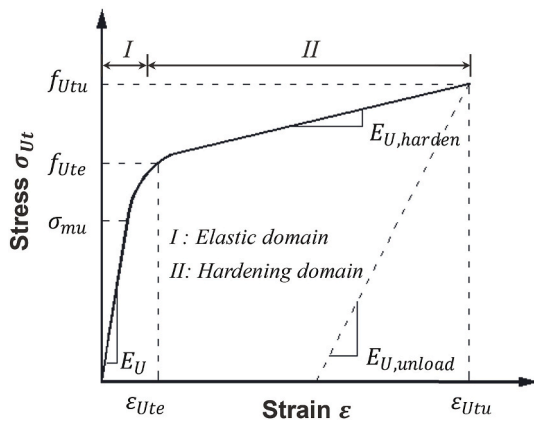Two major intertwined questions are currently open regarding the

---

**Fig. 1.** Typical stress-strain curve of strain-hardening UHPFRC, prior to the softening domain not shown here.

elastic limit of UHPFRC. The first one is how to determine it in a representative and reliable way. The second one is how to model the influence of the fibrous skeleton on the apparent elastic limit considering available literature data.

A reliable determination method should provide coherent results, which match the definition of elastic limit. As shown in Table 1, two types of test methods are usual for the determination of the elastic limit of UHPFRC, i.e., 4-point bending tests (4PBT) and uniaxial tensile tests (UTT). Related with different definitions and understandings, there are several determination methods for the elastic limit of UHPFRC under uniaxial tension.

Naaman [6] describes the first cracking of strain hardening fiber reinforced cement composites as a percolated crack, which completely separates the structural tensile member. The opening of the percolated crack may be very small and possibly invisible to the naked eye.

Adopting methods to determine modulus of elasticity of concrete and yield strength of steels, Makita and Brühwiler [8] first proposed an objective determination method, which provides coherent results. The elastic limit is determined as the intersection of the stress-strain curve and a line with slope equal to the modulus of elasticity and a strain offset of 0.1‰. El-Helou et al. [16] use the same approach while the strain offset of 0.2‰ is selected. In Refs. [5,17], the intersection of lines from linear fits of elastic and hardening domains is taken as the elastic limit. Graybeal and Baby [18,19] take the average load level at which cracking repeatedly occurs during the multi-cracking phase of UHPFRC as elastic limit.

Deformation modulus refers to the ratio of stress to corresponding strain during loading including elastic and inelastic behavior [20], which is commonly used to characterize the progressive degradation of materials as it is easy to determine. Relating the material properties to the deformation modulus provides an objective mean to determine the elastic limit. Based on the concept of decrease of deformation modulus, Denarié [21–23] first proposed an original method for the determination of the elastic limit of UHPFRC. This paper elaborates on that method with supplementary information, hereafter called modulus-drop method. Related with the determination procedure (Table 1), $f_{Ute,10\%}$ is used to denote the determined elastic limit.

This paper discusses the influence of fiber orientation on the elastic limit and compares three determination methods. It is found that fiber orientation has a significant influence on the matrix tensile strength, while this is not considered in current estimation equations of elastic limit [24,25]. An original relation model between fiber orientation and the elastic limit is thus proposed.

Further, five uniaxial tensile tests are conducted. First, the local fiber distribution in the specimens is determined using a magnetic probe. Afterward, the tests are conducted and monitored using three measurement techniques, i.e., linear variable displacement transducers

**Table 1**
Determination methods of the elastic limit of UHPFRC.

| References | Specimen | Testing method | Methodology of determination |
|---|---|---|---|
| [5,17] | Dumbbell | UTT, hinged/hinged supports | The elastic limit corresponds to the intersection of lines from linear fits of elastic and hardening domains. |
| [18,19] | Prisms of square cross section with tapered aluminum plates glued on opposite faces at each end of specimen | UTT, clamped, fixed/fixed supports | The average load level at which cracking repeatedly occurs during the multi-cracking phase is taken as the elastic limit. |
| [8] | Dumbbell | UTT, clamped, fixed/fixed supports | Line 1 is determined by stresses of 0.3 and 0.6 $f_{Ute,expected}$ on stress-strain curve. Line 2 is obtained with 0.1‰ strain offset of Line 1. Intersection of line 2 and stress-strain curve is the elastic limit. |
| [7] | Thick members – Prisms, size upon fiber length[a] | 4PBT | The elastic limit corresponds to the loss of linearity of the behavior in the force-deflection curve. |
| | Thin plates[b]: Annex E | | The amplitude of the linear domain $\Delta M$ on the moment-deflection curve is estimated visually. A straight line is drawn through $\Delta M/3$ and $2\Delta M/3$. The point where the experimental curve departs from the straight line is the elastic limit. |
| [22] | Dumbbell | UTT, clamped, fixed/fixed supports | The elastic limit corresponds to the stress where 10% decrease of the deformation modulus occurs, with respect to the value of deformation modulus for a stress level of 2 MPa at the elastic domain. |
| | Prisms with rectangular cross section | 4PBT | The elastic limit corresponds to the stress at the first point for which a 1% irreversible decrease of the deformation modulus occurs. |
| [27,28] | Two types of prisms upon fiber length | 4PBT | (1) The force-deflection curve is converted to the equivalent stress-deflection (σ-δ) curve. (2) The line passing by the origin of the σ-δ plot and corresponding to 75% of the initial tangent stiffness is drawn. (3) Its intersection with the σ-δ curve defines the point with coordinates 75% σ and 75% δ. (4) These two parameters are used to determine the elastic limit, with an empirical formula based on a statistical analysis of the results of numerous calculations of the bending response with a hinge model, for the considered geometry. |

*(continued on next page)*

**Table 1** (*continued*)

| References | Specimen | Testing method | Methodology of determination |
|---|---|---|---|
| [16] | Prisms of square cross section with tapered aluminum plates glued on opposite faces at each end of specimen | UTT, clamped, fixed/fixed supports | The elastic limit corresponds to the intersection of the stress-strain curve and a line with slope equal to the modulus of elasticity and a strain offset of 0.2‰. |

ᵃ The test specimens shall be prisms of square section a² and length 4a. The dimension a, between 7 cm and 20 cm, shall be between 5 and 7 times the length of the longest fibers. Elastic limit corrected by scale factor according to equation (D.2) is specified in Ref. [7].
ᵇ Specimens are sawn in large plates.

(LVDT), digital image correlation (DIC) and acoustic emission (AE). After tests, three objective methods are selected to determine the elastic limit of five specimens.

Based on the local fiber distribution, the proposed relation model is used to analyze the test results of matrix tensile strength and elastic limit. Based on the measurement results of LVDT, DIC and AE, the elastic limits determined with three methods are compared.

In this paper, matrix discontinuity, fictitious crack and real crack are used to describe the post-elastic fracture process following the tensile response of UHPFRC. The matrix discontinuities (micro-cracks invisible to naked eye) initiate and propagate in the late elastic domain and hardening domain. After the maximum tensile stress, a fracture process zone forms in the weakest zone of the tensile specimen and is defined as fictitious crack following the classical definition by Hillerborg [26]. A real crack in UHPFRC is reached when the crack opening reaches about half of the fiber length [4].

## 2. Effect of fiber orientation on elastic limit

### 2.1. Background

The tensile strength of UHPFRC $f_{Utu}$ can be estimated with equation (1) [4,5,24,29].

$$f_{Utu} = \mu_0 \mu_1 V_f \tau_f \frac{l_f}{d_f} \tag{1a}$$

$$\mu_0 = n_f \frac{A_f}{V_f} \tag{1b}$$

where fiber orientation coefficient $\mu_0$ is the probability that a fiber crosses a considered section, which can be obtained with equation (1b) [30–32]; $n_f$ is the number of fibers crossing a unit area; $A_f$ is the sectional area of a fiber; $V_f$ is the fiber volume fraction; fiber efficiency coefficient $\mu_1$ is the ratio between pull-out stress of an inclined fiber and that of a perfectly aligned one, which can be estimated based on the fiber orientation [14,33,34]; $\tau_f$ is the maximum fiber pull-out strength; $l_f$ and $d_f$ are the length and diameter of fibers, respectively.

To the authors' knowledge, there is no equation specifically for the estimation of the elastic limit of UHPFRC. Swamy and Mangat [35] use equation (2) to estimate the elastic limit of concrete reinforced with discontinuous steel fibers, which considers matrix tensile strength, the interfacial bond stress between fibers and matrix, fiber slenderness and volume fraction.

$$f_{Ute} = \sigma_{mu}\left(1 - V_f\right) + 0.82\tau_{first} V_f \frac{l_f}{d_f} \tag{2}$$

where $\sigma_{mu}$ is the matrix tensile strength; $\tau_{first}$ is the interfacial bond stress corresponding to the average bond stress when bond-slip commences.

Similarly, Naaman [24,25] uses equations (3a) and (3b) to estimate

the elastic limit of a fiber reinforced cement composite tensile specimen, while additionally considers the fiber orientation, contribution of bond at onset of matrix cracking, reduction of bond strength at fiber-matrix interface.

$$f_{Ute} = \sigma_{mu}\left(1 - V_f\right) + \alpha\tau V_f \frac{l_f}{d_f} \tag{3a}$$

$$\alpha = \alpha_1 \alpha_2 \alpha_3 \tag{3b}$$

where $\sigma_{mu}$ is the matrix tensile strength; $\alpha_1$ is the coefficient describing the average contribution of bond at onset of matrix cracking; $\alpha_2$ is the efficiency factor of fiber orientation in the uncracked state of the composite; $\alpha_3$ is the coefficient describing the reduction of bond strength at fiber-matrix interface; $\tau$ is the assumed average (also called equivalent) bond strength at the fiber-matrix interface.

In equation (3a), the elastic limit of a fiber reinforced cementitious composite tensile specimen is made up of contributions of the matrix and fibers. The fiber contribution is considered by the second term $\alpha\tau V_f \frac{l_f}{d_f}$. The matrix contribution is considered by the first term $\sigma_{mu}(1 - V_f)$, in which the matrix tensile strength $\sigma_{mu}$ is experimentally determined and assumed to be independent of reinforcing fiber parameters [24].

However, for UHPFRC, the experimental results show that the matrix tensile strength $\sigma_{mu}$ is significantly affected by the reinforcing fiber parameters especially the fiber orientation [13–15]. For two specimens made with the same UHPFRC material and curing condition, the ratio of their matrix tensile strength could be larger than 3 and so does the ratio of the elastic limit [13–15]. Therefore, equations (3a) and (3b) [24,25], which does not consider the influence of fiber parameters on the matrix tensile strength $\sigma_{mu}$, cannot be directly used to estimate the elastic limit of UHPFRC.

Further, given the contributions of matrix and fibers, i.e., the two terms in equation (3a) are both affected by the reinforcing fiber parameters, it would be possible to merge the two terms and develop a linear equation for the estimation of the elastic limit of UHPFRC, similar to the estimation equation of tensile strength, i.e., equation (1).

### 2.2. Compilation of literature data

Three different sets of literature data reporting on tensile test results using UHPFRC with different fiber orientation and mixes are considered: Nunes et al. [15], Maya Duque and Graybeal [13], Shen and Brühwiler [4].

For UHPFRC, the fiber orientation is mainly affected by the casting procedure, material properties at fresh state, fiber length and structure geometry [36,37]. Two approaches are usual to define the fiber orientation of UHPFRC. The first approach refers to the probability that a fiber crosses a considered section, with orientation coefficient $\mu_0$.

The second approach is related to the angle $\theta$ between a single fiber and the direction of principle tensile stress. As shown in equation (4), $\overline{\cos\theta_y}$ is defined as the average value of $\cos\theta$ of all fibers in a section, in which $n_f$ denotes the total number of fibers in the considered section.

**Table 2**
Fibrous mix of UHPFRC used in [4,13,15].

| Reference | Mix type | Fiber type | Volume fraction $V_f$ | Diameter $l_f$ | Length $d_f$ |
|---|---|---|---|---|---|
| [15] | Type I | Type A | 0.75% | 0.175 mm | 9 mm |
| | | Type B | 0.75% | 0.175 mm | 12 mm |
| | Type II | Type A | 1.5% | 0.175 mm | 9 mm |
| | | Type B | 1.5% | 0.175 mm | 12 mm |
| [13] | One type | One type | 2.0% | 0.2 mm | 12.7 mm |
| [4] | One type | One type | 3.8% | 0.175 mm | 13 mm |

**Table 3**
Summary of test results on average fiber orientation and elastic limit.

| References | Casting method | Specimen | $V_f$ | $\mu_{0,y}$ | $\overline{cos\,\theta_y}$ | $f_{Ute,estimated}$ (MPa) | $f_{Utu}$ (MPa) | $\mu_1$ | $\tau_f$ (MPa) | $f_{Ute}/f_{Ut}$ |
|---|---|---|---|---|---|---|---|---|---|---|
| [15] | Magnetically oriented to Y direction (principle tensile stress) | 1 | 3.0% | 0.81 | 0.93 | 9.65 | 16.47 | 1.00 | 11.3 | 0.47 |
| | | 2 | | 0.77 | 0.90 | 11.63 | 16.41 | 1.00 | 11.8 | 0.55 |
| | Not oriented | 3 | | 0.49 | 0.77 | 5.40 | 7.16 | 0.91 | 8.9 | 0.34 |
| | | 4 | | 0.51 | 0.74 | 4.63 | 7.19 | 0.91 | 8.6 | 0.30 |
| | Magnetically oriented to X direction | 5 | | 0.39 | 0.62 | 3.37 | 3.67 | 0.86 | 6.1 | 0.31 |
| | | 6 | | 0.28 | 0.56 | 2.88 | 3.18 | 0.72 | 8.7 | 0.18 |
| | Magnetically oriented to Y direction | 7 | 1.5% | 0.89 | 0.93 | 6.39 | 10.81 | 1.00 | 13.5 | 0.53 |
| | | 8 | | 0.83 | 0.90 | 5.67 | 7.7 | 1.00 | 10.3 | 0.61 |
| | Not oriented | 9 | | 0.65 | 0.75 | 2.31 | 4.12 | 0.97 | 7.3 | 0.35 |
| | Magnetically oriented to X direction | 10 | | 0.27 | 0.45 | 1.91 | 1.91 | 0.70 | 11.2 | 0.19 |
| | | 11 | | 0.18 | 0.41 | 1.43 | 1.43 | 0.47 | 18.9 | 0.08 |
| [13] | Extracted from 3000 × 1000 × 50 mm slabs cast from one end, cutting angles are with respect to flow direction. | $V_f$ | | Average of 3 specimens in each set | | Average of each specimen set (>40 specimens) | $f_{Utu}$ (MPa) | $\mu_1$ | $\tau_f$ (MPa) | $f_{Ute}/f_{Ut}^*$ |
| | | | | $\mu_{0,y}$ | $\overline{cos\,\theta_y}$ | $f_{Ute,reported}$ (MPa) | | | | |
| | 90° set | | 2.0% | 0.37 | 0.65 | 5.10 | 6.60 | 0.84 | 16.7 | 0.24 |
| | 45° set | | | 0.57 | 0.74 | 7.00 | 7.90 | 0.93 | 11.8 | 0.47 |
| | 0° set | | | 0.72 | 0.83 | 9.90 | 13.00 | 1.00 | 14.3 | 0.55 |
| [4] | Casting method | Specimen | $V_f$ | $\mu_{0,y}$ | | $f_{Ute,10\%}$ (MPa) | $f_{Utu}$ (MPa) | $\mu_1$ | $\tau_f$ (MPa) | $f_{Ute}/f_{Ut}^*$ |
| | Extracted from a 1100 mm × 1100 mm × 50 mm slab, cast in the center of formwork. | T1-1 | 3.8% | 0.68 | | 9.96 | 12.85 | 0.98 | 6.8 | 0.54 |
| | | T1-2 | | 0.62 | | 9.87 | 11.55 | 0.95 | 6.9 | 0.50 |
| | | T1-3 | | 0.53 | | 8.20 | 9.62 | 0.92 | 7.0 | 0.43 |
| | | T1-4 | | 0.53 | | 8.62 | 9.80 | 0.92 | 7.1 | 0.42 |
| | | T1-5 | | 0.52 | | 8.10 | 9.49 | 0.91 | 7.1 | 0.41 |
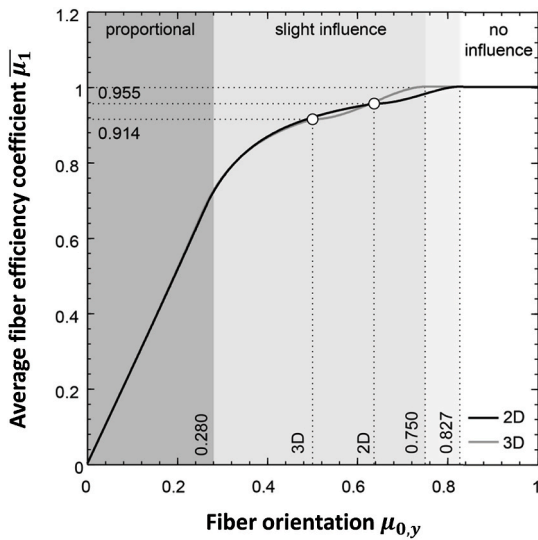


**Fig. 2.** Relation between fiber orientation and efficiency [30].



**Fig. 3.** Test results of fiber orientation and elastic limit.

The second approach does provide a better representation of the fiber orientation distribution than the first approach, but it is more time consuming and more sensitive to image analysis data accuracy as well as to the capabilities and limitations of the image analysis methodology [13,33].

$$\overline{cos\,\theta_y} = \frac{1}{n_f}\sum_{n=1}^{n_f} cos\,\theta_n \qquad (4)$$

Table 2 summarizes the fiber content of UHPFRC mixes used in Refs. [4,13,15]. Table 3 summarizes the test results of [4,13,15], which include the elastic limit and average fiber orientation coefficient in the direction of principle tensile stress (defined as Y direction in this paper) $\mu_{0,y}$. Based on Wuest's model describing the relation between fiber angle (with respect to the principle tensile direction) and fiber efficiency
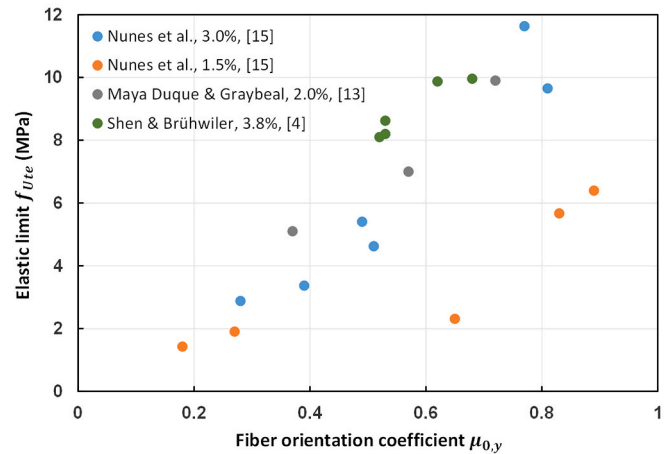
coefficient $\mu_1$ [38,39], Bastien Masse et al. further obtained the relation model between $\mu_{0,y}$ and $\mu_1$ [30] (Fig. 2). In Fig. 2 and D and 3D curves refer to two-dimensional and three-dimensional cases of fibers in the UHPFRC element, respectively. In Table 3, $\mu_1$ is determined using $\mu_{0,y}$ and the 3D relation model between $\mu_{0,y}$ and $\mu_1$ [30] (Fig. 2). The maximum fiber pull-out strength $\tau_f$ is calculated using equation (1a) [4, 5,24,29].

The maximum theoretical tensile strength $f_{Ut}^*$ is introduced as reference index among different literature data sets. It is defined by equation (5), which refers to the tensile strength of UHPFRC with one dimension orientation of fibers. Using $f_{Ut}^*$, the elastic limits of UHPFRC with different recipes in Refs. [4,13,15] are normalized to $f_{Ute}/f_{Ut}^*$ and given in Table 3.

$$f_{Ut}^* = \tau_f * \sum V_{fi} l_{fi} \big/ d_{fi} \qquad (5)$$

where $\tau_f$ is the maximum fiber pull-out strength, $\sum V_{fi}l_{fi}/d_{fi}$ is calculated with the volume fraction and aspect ratio of all fibers used in a UHPFRC mix.

Nunes et al. [15] use two types of UHPFRC and three casting methods to produce specimens. For every type of UHPFRC, every casting method is applied to produce six specimens, in which two specimens are further characterized to determine $\mu_{0,y}$ and $\overline{cos\,\theta_y}$. The present paper estimates the elastic limits of all the 36 specimens based on the stress-strain curves given in Ref. [15]. Without raw data, the elastic limits $f_{Ute,estimated}$ are visually determined as the point where a 10% deformation -modulus--drop happens.

In Maya Duque and Graybeal' study [13], prismatic specimens are cut from the slab at the angle of 0°, 45° and 90° with respect to the flow direction at casting. The reported average elastic limit of each specimen set $f_{Ute,reported}$ corresponds to the local maximum stress at the first crack [13]. For Shen and Brühwiler's research [4], five specimens are cut along the same direction from a slab, which is produced by pouring the fresh UHPFRC on the center of a rectangular formwork to fill the whole formwork. The present paper determines the elastic limits $f_{Ute,10\%}$ with the raw test data and the 10% modulus-drop method [21–23].

### 2.3. Model derivation

Fig. 3 shows the test results of average fiber orientation coefficient $\mu_{0,y}$ and elastic limit $f_{Ute}$ from Table 3. Among each series of data in Fig. 3, a linear relation is found between $\mu_{0,y}$ and $f_{Ute}$ when $\mu_{0,y}$ is in the range from about 0.25 to 0.88.

Martinie and Roussel [40] propose that fibers can be considered as fully oriented when they have an average angle of less than 20° with respect to the principle tensile direction. Besides, Fig. 2 describes the relation between fiber orientation $\mu_{0,y}$ and average efficiency $\overline{\mu_1}$. When $\mu_{0,y}$ is larger than 0.827, $\overline{\mu_1}$ is equal to 1.0, which means the fiber efficiency has no more influence on the tensile strength [14,38,39]. Thus, an upper limit of $\mu_{0,y}$ around 0.88 is suggested for the linear relation between fiber orientation and the elastic limit. When $\mu_{0,y}$ is larger than 0.88, the fibers are considered as fully oriented and the fiber orientation no longer has influence on the elastic limit.

When $\mu_{0,y}$-value is low, the fibers act like round or elliptic defects, perpendicular to the direction of principle tensile stress [14]. Consequently, with the decrease of $\mu_{0,y}$ to very low values, fracture mechanics mechanisms become more prominent [14,41]. This leads to high reduction of the elastic limit tensile stress and tensile strength. For specimen 11 with $\mu_{0,y}$ lower than 0.25 (Table 3) [15], the maximum fiber pull-out strength $\tau_f$ calculated is abnormally high. Thus, this data is not used and a lower limit of $\mu_{0,y}$ of 0.25 is assumed for the derivation of a linear relation between elastic limit and fiber orientation.

Based on the above, in order to build a better linear relation between the elastic limit and fiber orientation for $\mu_{0,y}$ between 0.25 and 0.88, the value of $f_{Ute}$ for the different data sets is normalized with respect to the parameter $f_{Ut}^*$. The results of fiber orientation coefficient $\mu_{0,y}$ and normalized elastic limit $r_{Ut} = f_{Ute}/f_{Ut}^*$ are shown in Fig. 4. After normalization, a linear relation is clearly found between $r_{Ut}$ and $\mu_{0,y}$, with a regression coefficient of 0.82. In the symbol $r_{Ut}$, $r$ denotes ratio, $U$ denotes UHPFRC, $t$ denotes tension.

Finally, the model between elastic limit and fiber orientation is proposed as follows.

- $0.88 \leq \mu_0 \leq 1.0 : r_{Ut} = 0.597$. The fibers are considered as fully oriented and the elastic limit is no longer affected by the fiber orientation.
- $0.25 \leq \mu_0 \leq 0.88 : r_{Ut} = 0.63\mu_{0,y} + 0.043$. The elastic limit increases with higher fiber orientation coefficient.
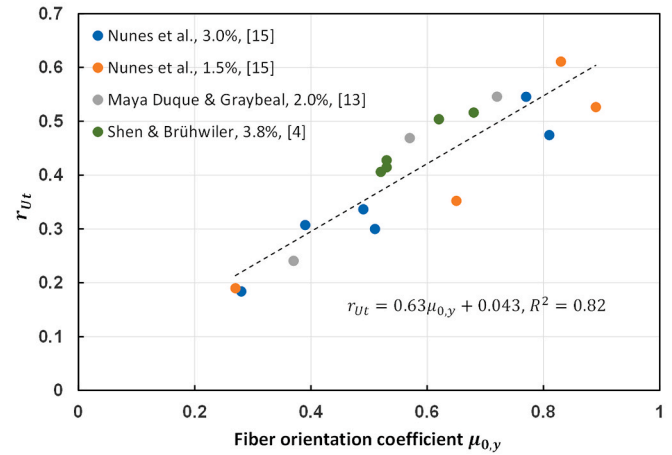


**Fig. 4.** Results of fiber orientation coefficient $\mu_{0,y}$ and $r_{Ut}$.

- $\mu_0 \leq 0.25 : r_{Ut} = 0.20$. According to linear elastic fracture mechanics, a round or elliptic defect in an infinite plate causes a stress concentration. The stress is locally increased by a factor of at least 3 compared to the globally applied stress [14,41,42]. The lower limit of 0.20, around 0.597 divided by 3, is thus taken to consider the influence of fiber orientation on the elastic limit.
- $f_{Ute} = r_{Ut} * f_{Ut}^*$. It is noted that $r_{Ut}$ is a global parameter describing the influence of fiber orientation on the elastic limit, which considers the influence of fiber orientation on the contribution of both matrix and fibers. It may not be considered as combination of $\alpha_1$, $\alpha_2$ and $\alpha_3$, only affecting the second term of equation (3a) [24,25].

## 3. Experimental campaign

### 3.1. Specimen design and preparation

The UHPFRC mix "Holcim 707" is used in this study. The fibrous mix is made of straight steel fibers with a length of 13 mm, diameter of 0.16 mm and dosage of 3.42 vol%. The water to cement ratio is 0.15. Composition of this mix is given in Table 4. The flow of freshly mixed UHPFRC [43–45] as well as the compressive strength and modulus of elasticity at three months of age are also given in Table 4.

As shown in Fig. 5, the dumbbell-shaped specimen is 750 mm-long with constant sections of 145 mm × 40 mm at central part and 200 mm × 40 mm at two heads. To avoid specimen failure at the transition zone, the Neuber's spline [46] is introduced to design the transition from the wide to narrow section, which is 50 mm-long. Besides, four tapered aluminum plates are glued on the specimen. These plates are 4 mm-thick and decrease linearly to 0.5 mm at the tip over a length of 50 mm [14].

Five specimens (QS-1 to 5) are cast horizontally in the formwork from one end to the other. The lateral internal faces of the molds along the shoulders are covered with 1-mm-thick deformable tapes to prevent built-in stress in the early age. The specimens are kept in the formworks for 2 days at room temperature of 20 ± 5 °C and then stored at room

**Table 4**
Composition and properties of UHPFRC.

| Components | Quantity (1 m³) | Properties | Average value |
|---|---|---|---|
| Premix | 1978 kg | Elastic modulus in compression | 46.7 GPa |
| Steel fibers ($l_f$ = 13 mm, $d_f$ = 0.16 mm, $V_f$ = 3.42%) | 268.0 kg | Compressive strength (cylinders) | 175.1 MPa |
| Superplasticizer (total) | 29.2 kg | Flow (spread after 25 blows) | 188 mm |
| Water | 175.8 kg | | |

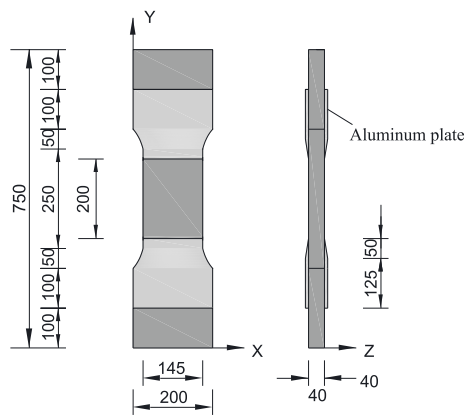**Fig. 5.** Specimen strengthened with aluminum plates (unit: mm).

temperature of 20 ± 5 °C under 100% RH for 1 week. Subsequently, specimens are stored in the laboratory until testing. Specimen age at testing is more than 90 days when over 90% of the UHPFRC final material properties are attained [47].

### 3.2. Uniaxial tensile tests

The tests have been conducted in a servo-hydraulic testing machine with a capacity of 1000 kN. Detailed test setup and instrumentation are shown in Fig. 6. The stroke-controlled mode is used with a displacement rate of 0.05 mm/min in the pre-peak domain and 0.1 mm/min in the post-peak domain.

In order to prevent bending effect and for easy specimen removal from the steel fixation, the specimen is installed in the testing machine by the approach of "gluing without bonding" proposed by Helbling and Brühwiler [48]. As shown in Figs. 6 and 7, a special metallic shoe with indented surfaces has been used to attach the specimen to the testing machine. The space between the XY plane of the specimen and the steel device is filled out with epoxy resin. Through interlocking, the tensile loading is introduced to the specimen by the resin. To avoid bonding between the specimen and the steel shoe, demolding spray is applied on the steel shoe surfaces before applying the resin on the specimen and the steel shoe surfaces.

The attachment system fully fixes the specimen at both ends and guarantees a uniform stress transfer without lateral restraint. It has no hinge and is built such that the specimen is fully restrained in-plane and out-of-plane. Full fixity has been verified by suitability tests that are not reported in this paper [48]. Between the two fixed ends of the specimen,
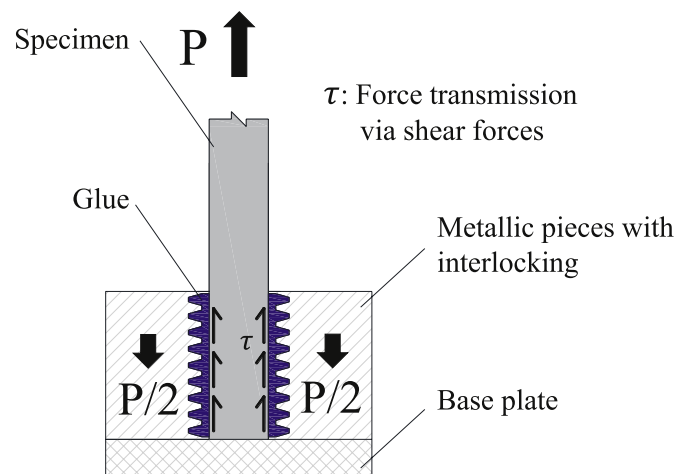


**Fig. 7.** Fixture of the tensile specimen in the testing machine.

the investigated central part of the specimen may show local bending effects due to varying local fiber distributions in the bulk material of the specimen. These effects are considered being inherent to UHPFRC.

Three measurement techniques are used during testing, i.e., linear variable displacement transducers (LVDT), digital image correlation (DIC) and acoustic emission (AE). Two LVDTs with a measurement base length of 200 mm are attached on both YZ plane of the specimen to measure the deformation over the central part of the specimen. The LVDT recording frequency is 10 Hz.

The DIC technique is used to monitor the entire testing process of one specimen surface. The targeted area is 145 mm × 200 mm on the central part of the specimen surface. The measurement accuracy is 0.003 mm. The recording frequency is 2 Hz. The DIC images are analyzed using the software Vic-3D after testing.

As shown in Fig. 6, eight acoustic emission sensors are symmetrically mounted on the casting and sheathed surfaces of the specimen respectively. Following the NF EN 1330-9 standard [49], pencil-lead break tests are conducted to check the mounting quality and to build the attenuation profile. Detection threshold and band filter are set as 42 dB and between 110 MHz and 400 MHz respectively. During testing, the AE-feature data and transient data are both collected at the sampling rate of 10 MHz.
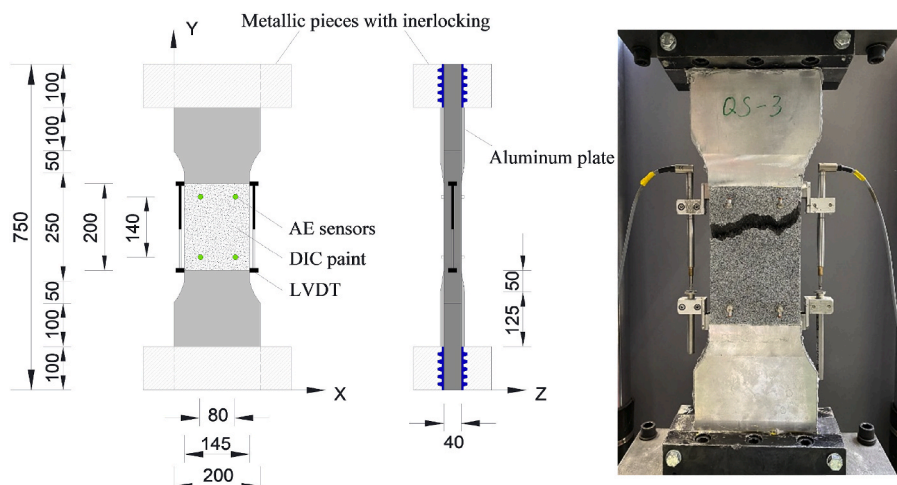


**Fig. 6.** Test setup and instrumentation (unit: mm).

### 3.3. Fiber distribution measurement

For UHPFRC using steel fibers, the fiber distribution (local dosage and orientation) inside the specimen can be determined with magnetoscopy [4,50,51]. Before testing, the measurement is conducted on specimens QS-1 to 4 using the Agilent E4980A LCR Meter with a magnetic probe (Fig. 8) [15,50]. For the LCR Meter, the test frequency is 20 Hz and the signal level is 2 V. The effective penetration depth of the magnetic probe is around 25 mm [51,52].

As shown in Fig. 8, the measurement is conducted on the central part of the specimen for both casting and sheathed surfaces. For each surface, 18 measurement points are selected, i.e., points A1 to 9 and points B1 to 9. The point spacing are 26 mm in X direction and 30 mm in Y direction.

During measurement, the probe center is placed on each point. The magnetic inductance along X and Y directions, i.e., $L_x$ and $L_y$ are obtained by putting the long side of the probe perpendicular to the X and Y direction respectively. The inductance in the air is defined as $L_{air}$. The relative magnetic permeability in X and Y directions is then given by $\mu_{r,x} = L_x/L_{air}$ and $\mu_{r,y} = L_y/L_{air}$. The fiber distribution of each rectangle on the specimen is determined by the relative magnetic permeability of the point within the rectangle. Rectangles A 1 to 9 on the casting surface have the same X and Y coordinates as the rectangles B 1 to 9 on the sheathed surface and vice versa.

## 4. Analysis of stress – strain response

### 4.1. Methods of determination of elastic limit

#### 4.1.1. Deformation modulus-drop

The modulus-drop method is graphically shown in Fig. 9. Point $A_0$ represents the point where a significant decrease of the deformation modulus is noticeable. Points 2, 3, $A_0$ and $A_{10\%}$ on the stress-strain curve correspond to points 2′, 3′, $A_0'$ and $A_{10\%}'$ on the deformation modulus curve. Based on [22,53], the methodology is elaborated as follows:

I. The deformation modulus $E_i$ is determined as the slope of the line comprising one fixed point, point 1, and the current point i on the stress-strain curve. In order to avoid local variations due to noise of measurement equipment, the moving average of the deformation modulus $E_{im}$ over the last 10 points (points i-9 to point i) is introduced. To mitigate nonlinear effects at the test beginning (which is mainly due to the test setup), point 1 should be as low as
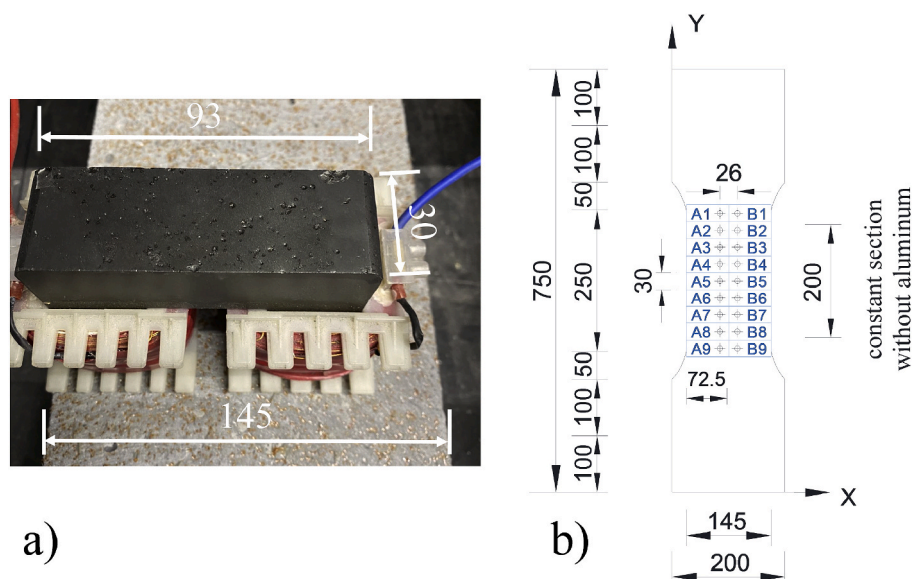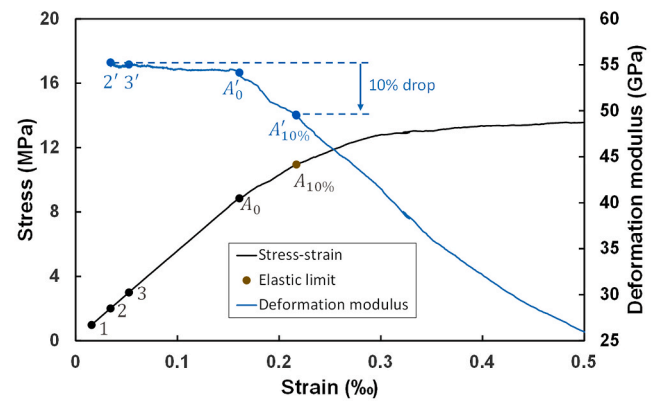


**Fig. 9.** Graphical representation of modulus-drop method.

possible but following the trend line of the initial part of stress-strain curve. The default point is set at 0.5 MPa. All the deformation modulus curves plotted in subsequent figures in the present paper refer to moving average (10 last points) deformation modulus $E_{im}$.

II. $E_{im}$ at the stress level of 2 MPa, i.e., at point 2′ is taken as the reference modulus. To obtain representative values of the elastic limit, for curves of $E_{im}$ with large variation around point 2′, the average value of all $E_{im}$ between points 2′ and 3′ could be taken as the reference modulus. Point 3′ corresponds to a stress level where the value of $E_{im}$ does not decrease notably and is before point $A_0'$, e.g. the point at the deformation modulus curve corresponding to the stress level of 3 MPa.

III. On the deformation modulus (moving average) - strain curve, the point with a deformation modulus $E_{im}$ of 90% of the reference modulus (10% decrease) is marked as point $A_{10\%}'$. Accordingly, point $A_{10\%}$ on the stress-strain curve is defined as the elastic limit, which yields $f_{Ute,10\%}$.

Prerequisites for a proper determination of the elastic limit are: appropriate test setup and calibration of measurement devices; specimen eccentricity which needs to be checked with displacement transducer measurements; experimental data appropriately collected for applying this method (sampling frequency larger than 5 Hz).
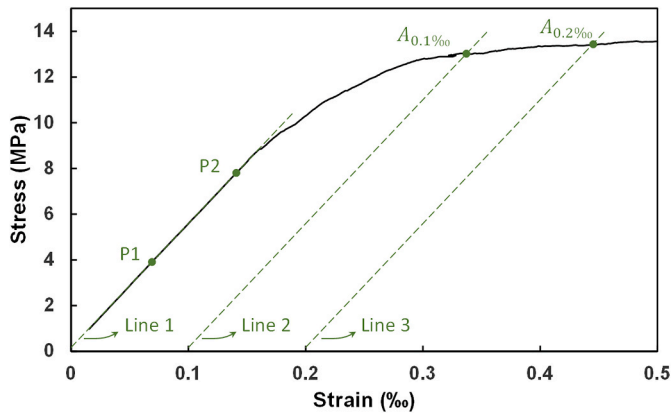


**Fig. 8.** Magnetic measurement: a) measurement on the $L_y$ of rectangle $A_i$; b) measurement points (unit: mm).

**Fig. 10.** Graphical representation of two strain-offset methods.

### 4.1.2. Strain-offset

Two strain-offset methods [8,16] are graphically shown in Fig. 10. The reference line, i.e. line 1, is the linear-elastic part of the stress-strain curve. Lines 2 and 3 are parallel to line 1 with a strain-offset of 0.1‰ and 0.2‰, respectively. The two intersections of the stress-strain curve and

lines 2 and 3, i.e. points $A_{0.1‰}$ and $A_{0.2‰}$ are defined as the elastic limits $f_{Ute,0.1‰}$ and $f_{Ute,0.2‰}$ respectively. According to Ref. [8], line 1 is determined by points P1 and P2, which correspond to stress levels of 30% and 60% of the expected elastic limit $f_{Ute,expected}$ on the stress-strain curve. According to Ref. [16], line 1 starts from the origin of the stress-strain curve and has a slope equal to the elastic modulus.

### 4.2. Application to the tensile test data and discussion

Fig. 11 shows the deformation modulus- and stress-strain curves of five uniaxial tensile specimens from test beginning to early hardening domain, while Fig. 12 shows the stress – strain curves from test beginning to early softening domain. Table 5 summarizes the values of stress and strain at tensile strength and elastic limit determined by three methods.

The strain is calculated based on the average reading of the two LVDTs and measurement base length, while the stress is calculated as measured force divided by the sectional area. The elastic limits $f_{Ute,10‰}$, $f_{Ute,0.1‰}$ and $f_{Ute,0.2‰}$ are respectively determined using the modulus-drop method [22,53] and the two strain-offset methods [8,16] explained above. The tensile strength $f_{Utu}$ is defined as the maximum stress reached during the test [9].

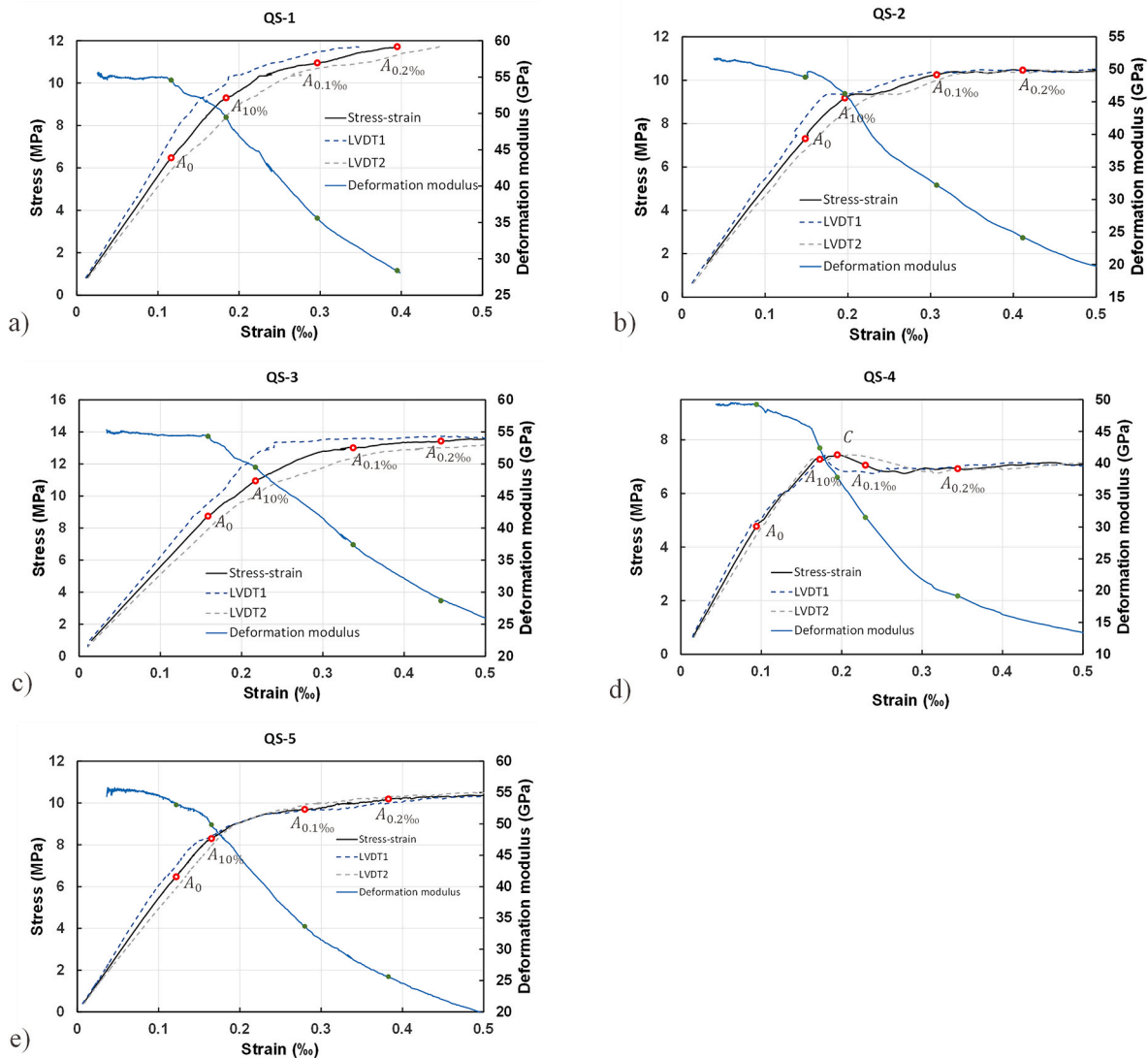In Fig. 11, point $A_0$ represents the point where a significant decrease



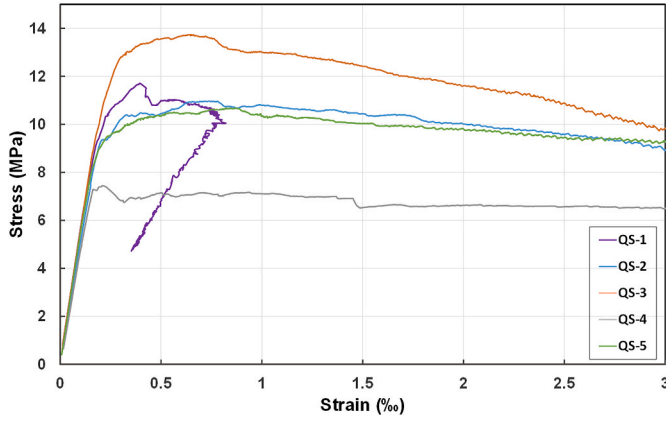**Fig. 11.** Deformation modulus- and stress-strain curves of specimens QS-1 to 5, a) to e).

**Fig. 12.** Stress-strain curves of specimens QS-1 to 5.

to develop resistance and obtain strain hardening behavior after matrix discontinuities occurred [54].

Based on the discussion above, it may be concluded that the two strain-offset methods significantly overestimate the elastic limit of UHPFRC. It is noted that specimen QS-1 has premature failure slightly outside the LVDT measurement base length in the strain hardening domain, leading to unreliable LVDT measurement results after the strain of 0.4‰ and specimen fracture near the bottom right of the DIC measurement surface. While before the maximum stress, no matrix discontinuity is observed at that failure region according to DIC results later in this paper, and the deformation modulus- and stress-strain curves also develop normally. Thus, the elastic limit of specimen QS-1 is not considered to be affected by an abnormal failure.

## 5. Discussion on local fiber distribution and elastic limit

### 5.1. Determination of local fiber distribution

Before testing, the relative magnetic permeability ($\mu_{r,x}$ and $\mu_{r,y}$) of 36 rectangular zones (72.5 mm × 30 mm) in the central specimen part (Fig. 8) are measured for specimens QS-1 to 4. Based on the measurement results, the fiber volume and orientation in each zone, hereafter called local fiber distribution, are determined using equation (6). In the present research, the same set of equations from Shen and Brühwiler's work [4] are adopted because a similar UHPFRC mix and the same magnetic probe are used [15].

$$\mu_{r,mean} = \left(\mu_{r,x} + \mu_{r,y}\right)/2 \tag{6a}$$

$$V_f = \left(\mu_{r,mean} - 1\right)/4.55 \tag{6b}$$

$$\left(\rho_x - \rho_y\right) = 0.5 \frac{\mu_{r,x} - \mu_{r,y}}{\mu_{r,mean} - 1} \tag{6c}$$

$$\mu_{0,y} = 0.57 + 1.85\left(\rho_x - \rho_y\right) \tag{6d}$$

where $\mu_{r,mean}$ is the mean relative magnetic permeability; $\mu_{r,x}$ and $\mu_{r,y}$ are the relative magnetic permeability in X and Y directions; $(\rho_x - \rho_y)$ is the fiber orientation indicator; $\mu_{0,y}$ is the fiber orientation coefficient in the direction of principle tensile stress.

### 5.2. Analysis of local fiber distribution

As shown in Figs. 13 and 14, the local fiber distribution, i.e., fiber volume fraction $V_f$ and orientation coefficient $\mu_{0,y}$ of each zone are presented for specimens QS-1 to 4. As proposed in section 2, the elastic limit can be theoretically calculated by $f_{Ute} = r_{Ut}\tau_f V_f \frac{l_f}{d_f}$, in which the relation between $r_{Ut}$ and $\mu_0$ is linear when $\mu_0$ is between 0.25 and 0.88. Here, parameter $\lambda = r_{Ut} V_f \frac{l_f}{d_f}$ is introduced to analyze the combining influence of local fiber distribution on the elastic limit (Fig. 15). The overall results are summarized in Table 6, in which $\widehat{c}_v$ is the coefficient of variation.

of the deformation modulus is noticeable. Points $A_{10\%}$, $A_{0.1‰}$ and $A_{0.2‰}$ correspond to $f_{Ute,10\%}$, $f_{Ute,0.1‰}$ and $f_{Ute,0.2‰}$ respectively. Point C corresponds to the tensile strength $f_{Utu}$. Point B is avoided throughout this paper.

For specimens QS-1 to 5, the stress levels at point $A_0$ are 6.48 MPa, 7.31 MPa, 8.75 MPa, 4.78 MPa and 6.47 MPa, respectively. At point $A_0$, each stress-strain curve shows a small oscillation and then the deformation modulus starts to decrease quickly. This could indicate that matrix discontinuities start to form from point $A_0$ and the according stress level can be taken as the matrix tensile strength $\sigma_{mu}$. This analysis is validated by the measurement results of DIC and AE later in this paper.

For specimens QS-1 to 5, points $A_{0.1‰}$ all lie after points $A_{10\%}$ and have deformation modulus decreases of 35%, 37%, 32%, 36% and 40% respectively. For specimen QS-4, point $A_{0.1‰}$ even lies after the tensile strength, i.e., point C. Lying after points $A_{0.1‰}$, points $A_{0.2‰}$ of specimens QS-1 to 5 are in the early hardening domain, and the deformation modulus decreases are 48%, 51%, 48%, 61% and 54% respectively.

As shown in Table 5 and Figs. 11 and 12, specimens QS-1 to 3 and 5 exhibit strain hardening behavior. The tensile strengths $f_{Utu}$ range from 10.68 MPa to 13.74 MPa. The elastic limits $f_{Ute,10\%}$ range from 8.30 MPa to 10.95 MPa with $\varepsilon_{Ute,10\%}$ ranging from 0.17‰ to 0.22‰. While $f_{Ute,0.1‰}$ are all higher, ranging from 9.70 MPa to 13.02 MPa, close to the tensile strengths. $f_{Ute,0.2‰}$ are higher than $f_{Ute,0.1‰}$, ranging from 10.20 MPa to 13.43 MPa. The average ratio of $f_{Ute,10\%}$, $f_{Ute,0.1‰}$ and $f_{Ute,0.2‰}$ to $f_{Utu}$ are 0.84, 0.94 and 0.96 respectively. The differences between $f_{Ute,0.1‰}$ and $f_{Utu}$ are all less than 0.75 MPa. The differences between $f_{Ute,0.2‰}$ and $f_{Utu}$ are all less than 0.51 MPa.

As shown in Table 5 and Figs. 11 d) and 12, specimen QS-4 exhibits no strain hardening behavior. The tensile strength is only 7.44 MPa with a strain of 0.19‰. Beyond tensile strength, the stress quickly drops to 6.75 MPa. The elastic limit $f_{Ute,10\%}$ is 7.28 MPa with a strain of 0.17‰. Points $A_{0.1‰}$ and $A_{0.2‰}$ lie after point C and their stress levels are 7.05 MPa and 6.92 MPa respectively. These could be because the fiber distribution at the weakest region of the specimen is too unfavorable, probably due to a defect during material mixing or specimen fabrication,

**Table 5**
Tensile properties of specimens QS-1 to 5.

| Test | $f_{Ute,10\%}$ (MPa) | $f_{Ute,0.1‰}$ (MPa) | $f_{Ute,0.2‰}$ (MPa) | $f_{Utu}$ (MPa) | $\dfrac{f_{Utu}}{f_{Ute,10\%}}$ | $\varepsilon_{Ute,10\%}$ | $\varepsilon_{Ute,0.1‰}$ | $\varepsilon_{Ute,0.2‰}$ | $\varepsilon_{Utu}$ |
|------|------|------|------|------|------|------|------|------|------|
| QS-1 | 9.31 | 10.95 | 11.70 | 11.72 | 1.26 | 0.19‰ | 0.30‰ | 0.41‰ | 0.40‰[a] |
| QS-2 | 9.18 | 10.24 | 10.46 | 10.97 | 1.19 | 0.20‰ | 0.31‰ | 0.41‰ | 0.75‰ |
| QS-3 | 10.95 | 13.02 | 13.43 | 13.74 | 1.25 | 0.22‰ | 0.34‰ | 0.45‰ | 0.65‰ |
| QS-4 | 7.28 | 7.05 | 6.92 | 7.44 | 1.02 | 0.17‰ | 0.23‰ | 0.34‰ | 0.19‰ |
| QS-5 | 8.30 | 9.70 | 10.20 | 10.68 | 1.29 | 0.17‰ | 0.28‰ | 0.39‰ | 0.87‰ |

[a] Specimen QS-1 has premature failure beyond LVDT measurement base length, leading to inaccurate value of $\varepsilon_{Utu}$.
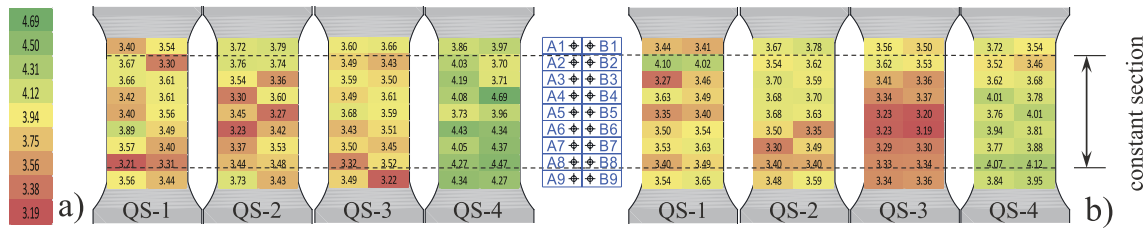
**Fig. 13.** Local fiber volume fraction $V_f$: a) casting surface; b) sheathed surface (unit: %).
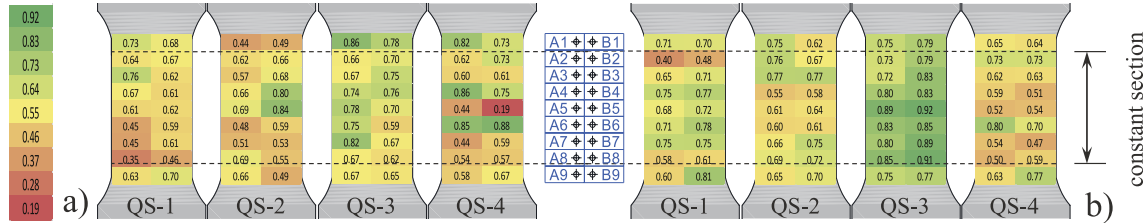


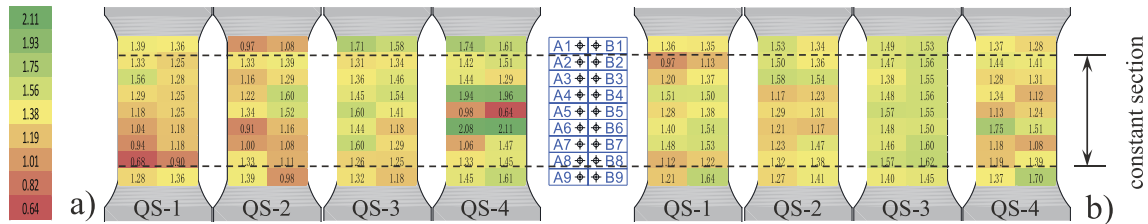**Fig. 14.** Local fiber orientation coefficient $\mu_{0,y}$: a) casting surface; b) sheathed surface.



**Fig. 15.** Local fiber distribution parameter $r_{Ut}V_f\frac{l_f}{d_f}$: a) casting surface; b) sheathed surface.

**Table 6**
Summary of the fiber distribution (average and coefficient of variation).

| Items | QS-1 | | | QS-2 | | | QS-3 | | | QS-4 | | | Total |
|---|---|---|---|---|---|---|---|---|---|---|---|---|---|
| | casting | sheathed | average | casting | sheathed | average | casting | sheathed | average | casting | sheathed | average | |
| $V_f$ (%) | 3.50 | 3.55 | 3.52 | 3.51 | 3.56 | 3.53 | 3.50 | 3.36 | 3.43 | 4.14 | 3.81 | 3.97 | 3.62 |
| $\widehat{c_v}$ | 4.6% | 5.9% | 5.3% | 5.1% | 3.9% | 4.5% | 3.2% | 3.7% | 4.0% | 6.9% | 5.0% | 7.3% | 8.0% |
| $\mu_{0,y}$ | 0.60 | 0.68 | 0.64 | 0.61 | 0.67 | 0.64 | 0.71 | 0.82 | 0.76 | 0.64 | 0.62 | 0.63 | 0.67 |
| $\widehat{c_v}$ | 18.1% | 16.0% | 17.7% | 18.2% | 10.2% | 15.1% | 9.9% | 7.4% | 10.9% | 27.3% | 15.5% | 22.1% | 18.3% |
| $\lambda$ | 1.21 | 1.35 | 1.28 | 1.22 | 1.35 | 1.28 | 1.40 | 1.51 | 1.46 | 1.50 | 1.34 | 1.42 | 1.36 |
| $\widehat{c_v}$ | 17.0% | 13.1% | 15.8% | 16.2% | 9.7% | 13.9% | 10.9% | 4.3% | 8.8% | 25.4% | 13.6% | 21.6% | 16.7% |

Specimens QS-1 to 4 are cast horizontally in the formwork from one end to the other. Shen and Brühwiler [4] also determined the local fiber distribution of five dumbbell-shaped specimens. The specimens consist of a same UHPFRC matrix with fiber content of 3.8 vol%, fibers length of 13 mm and fiber diameter of 0.175 mm. The specimens are fabricated in a different way. The fresh UHPFRC is poured on the center of a square formwork (1100 mm × 1100 mm × 50 mm) to fill the whole formwork. After demolding, specimens are cut from the large slab element. The local fiber distribution and test results of specimens from the two research are compared below.

As shown in Table 6, the average $V_f$ of QS-1 to 3 are from 3.43% to 3.53%, close to the assumed mix-design value 3.42%. However, the average $V_f$ of QS-4 is 3.97%, much higher than 3.42%. The average $V_f$ of the casting surface is smaller than that of the sheathed surface for QS-1 and 2, while larger for QS-3 and 4. This could be a strong indication that the fresh UHPFRC has no segregation, otherwise the average $V_f$ would be all larger at the sheathed surface. The $\widehat{c_v}$ of $V_f$ of four specimens is 8.0%, close to 10.7% of Shen and Brühwiler's slab [4].

The average $\mu_{0,y}$ of specimens QS-1 to 4 is 0.67, larger than 0.58, the

average $\mu_{0,y}$ of Shen and Brühwiler's five specimens cut from a slab [4]. This is because the casting method used in this study contributes to a more favorable fiber orientation [15,55].

For specimens QS-1 to 4, the average $\mu_{0,y}$ are 0.64, 0.64, 0.76 and 0.63 and their $\widehat{c_v}$ are 17.7%, 15.1%, 10.9% and 22.1% respectively. For each specimen, $\widehat{c_v}$ of the casting surface is always higher than that of the sheathed surface, which is also found in Shen and Brühwiler's results [4]. This can be explained by the wall effect [15]. Consequently, the lowest values of $\mu_{0,y}$, i. e, the weakest local fiber orientation are all found at the casting side, which are respectively 0.35, 0.44, 0.59 and 0.19 for QS-1 to 4. For $\mu_{0,y}$ of specimen QS-4, the second lowest value is 0.44 and the minimum value of 0.19 is an outlier, probably due to a defect during material mixing or specimen fabrication.

$\lambda = r_{Ut}V_f\frac{l_f}{d_f}$ shows similar distribution to $\mu_{0,y}$. The average $\lambda$ of four specimens is 1.36. For specimens QS-1 to 4, the average $\lambda$ are 1.28, 1.28, 1.46 and 1.42 and their $\widehat{c_v}$ are 15.8%, 13.9%, 8.8% and 21.6% respectively. For each specimen, $\widehat{c_v}$ of the casting surface is always higher than that of the sheathed surface. As a result, the lowest values of $\lambda$ are all

found at the casting side, which are respectively 0.68, 0.91, 1.18 and 0.64 for specimens QS-1 to 4.

In the proposed linear relation model in section 2.2.2, $r_{Ut}$ is taken as 0.20 when $\mu_{0,y}$ is less than 0.25. When $\mu_{0,y}$ is lower than 0.25, the stress concentration at local defects becomes prominent [14,41] and the linear relation is no longer applicable. Among the four specimens, only QS-4 has one zone with $\mu_{0,y}$ lower than 0.25, which is 0.19 and leads to the lowest λ of 0.64. Thus, the elastic limit of specimen QS-4 could be much lower than QS-1, although the lowest λ of specimens QS-1 is 0.68.

### 5.3. Influence of local fiber distribution on elastic limit

As determined before, the stress levels of point $A_0$ are taken as matrix tensile strength $\sigma_{mu}$ and are equal to 6.48 MPa, 7.31 MPa, 8.75 MPa and 4.78 MPa respectively for specimens QS-1 to 4. While the elastic limit stresses $f_{Ute,10\%}$ are 9.31 MPa, 9.18 MPa, 10.95 MPa and 7.29 MPa respectively.

For specimen QS-3, $\sigma_{mu}$ and $f_{Ute,10\%}$ are 8.75 MPa and 10.95 MPa, highest among the four specimens. Accordingly, it has highest average values of $\mu_{0,y}$ and λ, i.e., 0.76 and 1.46. Besides, QS-3 also has lowest $\widehat{c_v}$ of $\mu_{0,y}$ and λ, i.e., 10.9% and 8.8%.

$\sigma_{mu}$ and $f_{Ute,10\%}$ of specimens QS-1 and 2 are lower than those of QS-3, while close to each other. Their $\sigma_{mu}$ are 6.48 MPa and 7.31 MPa, while the $f_{Ute,10\%}$ are 9.31 MPa and 9.18 MPa. Accordingly, the two specimens have the same average $\mu_{0,y}$ of 0.64 and same average λ of 1.28 respectively, all lower than those of QS-3. For QS-1 and 2, the $\widehat{c_v}$ of $\mu_{0,y}$ are 17.7% and 15.1%, while the $\widehat{c_v}$ of λ are 15.8% and 13.9%. Rectangle A8 on the casting surface of QS-1 has the lowest values of $\mu_{0,y}$ and λ in this specimen, i.e., 0.35 and 0.68, which explains the reason that specimen QS-1 fails near this rectangle, slightly outside the LVDT measurement base length.

The average $\mu_{0,y}$ of specimen QS-4 is 0.63, close to 0.64 of specimens QS-1 and 2. The average λ of specimen QS-4 is 1.42, higher than 1.28 of specimens QS-1 and 2, and lower than 1.46 of specimen QS-3. While $\sigma_{mu}$ and $f_{Ute,10\%}$ of specimen QS-4 are only 4.78 MPa and 7.29 MPa, much smaller than those of the other three specimens. This is because of the outlier, rectangle B5 on the casting surface of specimen QS-4, whose $\mu_{0,y}$ and λ are only 0.19 and 0.64. For the three other specimens, the lowest $\mu_{0,y}$ and λ are 0.35 and 0.68. Besides, specimen QS-4 also has the highest $\widehat{c_v}$ of $\mu_{0,y}$ and λ among four specimens, i.e., 22.1% and 21.6%.

### 5.4. Elastic limits from tests results and model

Table 7 provides the test results from the present study and [4], which use the same matrix and similar fibers. $f_{Utu}$, $f_{Ute,10\%}$ and $\mu_0$ are directly determined from test results. $V_f \frac{l_f}{d_f}$, $\mu_1$ and $\tau_f$ are determined following the same procedures introduced in section 2.2. The coefficient $r_{Ut}$ is determined based on the proposed relation model between $\mu_0$ and $r_{Ut}$. Then, the theoretical elastic limit $f_{Ute,cal} = r_{Ut}\tau_f V_f \frac{l_f}{d_f}$ is obtained.
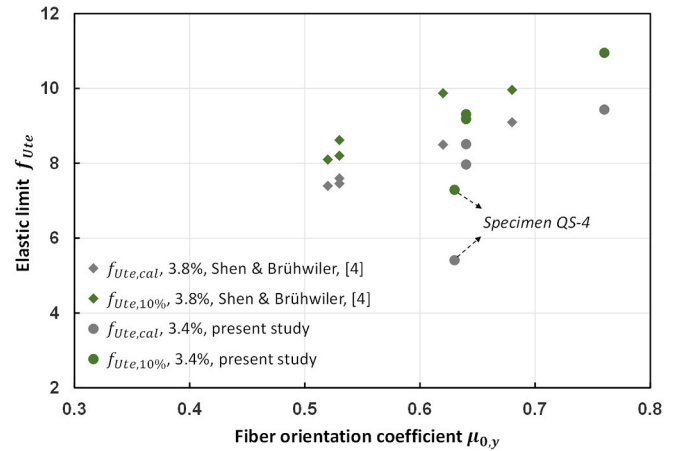


**Fig. 16.** Fiber orientation and elastic limit from model and test results.

Furthermore, Fig. 16 shows the results of fiber orientation and elastic limit obtained from calculation and tests.

As shown in Table 7 and Fig. 16, all the estimated elastic limits $f_{Ute,cal}$ are close to while lower than the test results $f_{Ute,10\%}$. The difference between $f_{Ute,cal}$ and $f_{Ute,10\%}$ is 1.88 MPa for specimen QS-4, which has a rectangle with extremely low $\mu_0$ of 0.19. For the other 8 specimens, the differences are between 0.70 MPa and 1.52 MPa. And their elastic limits from calculation and tests both clearly show linear relation with the average $\mu_0$.

The specimen QS-4 is an exception. Although the average $\mu_{0,y}$ of specimen QS-4 is 0.63, close to 0.64 of specimens QS-1 and 2, its elastic limit is much lower than those of other two specimens. This shows that the extremely poor fiber orientation at a local zone leads to a sharp decrease for the elastic limit since in a uniaxial tensile test, the properties of the weakest zone always determines the specimen response. Nevertheless, the conclusion is still obtained that the elastic limit can be appropriately estimated using the proposed relation model and the average fiber orientation results. The test results of specimens QS-6 to 14 in appendix A further validate this conclusion.

## 6. Discussion on DIC and AE results

### 6.1. Measurement results

Fig. 17 a) to 20 a) and Fig. 21 present the tensile response of specimens QS-1 to 5 as characterized by LVDT and DIC, showing close results of stress-deformation curves. The polished surface of specimen QS-2 and the sheathed surface of the other 4 specimens are used for the DIC surface. DIC images showing the strain contour are presented for key points on the stress-strain curve obtained from LVDT measurement. Points $A_0$, $A_{10\%}$, $A_{0.1‰}$, $A_{0.2‰}$ and C are the same as defined in section 4.2. Point D is a point in the softening domain where the fictitious crack is well

**Table 7**
Elastic limit obtained from tests and calculation.

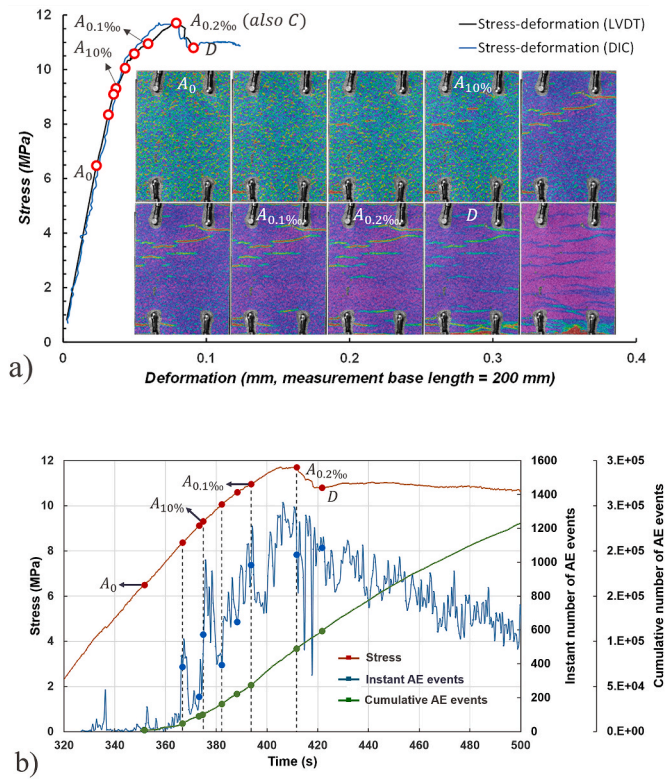| Reference | Specimen | $V_f \frac{l_f}{d_f}$ | $\mu_{0,y}$ | $\mu_1$ | $\tau_f$ (MPa) | $r_{Ut} = \frac{f_{Ute,10\%}}{f^*_{Ut}}$ | $f_{Utu}$ (MPa) | $f_{Ute,10\%}$ (MPa) | $f_{Ute,cal}$ (MPa) |
|---|---|---|---|---|---|---|---|---|---|
| Shen and Brühwiler [4] | T1-1 | 2.82 | 0.68 | 0.98 | 6.83 | 0.47 | 12.85 | 9.96 | 9.09 |
| | T1-2 | 2.82 | 0.62 | 0.95 | 6.94 | 0.43 | 11.55 | 9.87 | 8.50 |
| | T1-3 | 2.82 | 0.53 | 0.92 | 7.01 | 0.38 | 9.62 | 8.20 | 7.46 |
| | T1-4 | 2.82 | 0.53 | 0.92 | 7.14 | 0.38 | 9.80 | 8.62 | 7.60 |
| | T1-5 | 2.82 | 0.52 | 0.91 | 7.07 | 0.37 | 9.49 | 8.10 | 7.40 |
| Present study | QS-1 | 2.76 | 0.64 | 0.96 | 6.91 | 0.45 | 11.72 | 9.31 | 8.51 |
| | QS-2 | 2.76 | 0.64 | 0.96 | 6.46 | 0.45 | 10.97 | 9.18 | 7.97 |
| | QS-3 | 2.76 | 0.76 | 1.00 | 6.54 | 0.52 | 13.74 | 10.95 | 9.43 |
| | QS-4 | 2.76 | 0.63 | 0.96 | 4.45 | 0.44 | 7.44 | 7.29 | 5.41 |

**Fig. 17.** Experimental characterization of QS-1: a) DIC analysis of sheathed surface; b) AE analysis.

developed. And it corresponds to a local discontinuity on the DIC strain contour, i.e., a zone where the strain contour is no more available.

When materials are subjected to stress and fail on a microscopic scale, energy is released to generate transient elastic stress waves. The AE technique collects and processes these stress waves [56,57]. By means of numbers of instant and cumulative AE events, the formation and propagation of matrix discontinuities and the fictitious crack, fiber pull-out and fracture inside the UHPFRC tensile specimen can be quantified in real time [17,53,58,59].

In Fig. 17 b) to 20 b), instant and cumulative AE event numbers are plotted in real time for specimens QS-1 to 4. Besides, AE event numbers at the elastic limits determined by the three methods, i.e., points $A_{10\%}$, $A_{0.1‰}$ and $A_{0.2‰}$, are given in Table 8.

### 6.2. Matrix tensile strength

As analyzed in section 4.2, point $A_0$ is the turning point where a

**Table 8**
AE event numbers at points $A_{10\%}$, $A_{0.1‰}$ and $A_{0.2‰}$.

| Specimen | Point | Stress (MPa) | Instant event (−) | Cumulative event (−) |
|---|---|---|---|---|
| QS-1 | $A_{10\%}$ | 9.31 | 573 | 18781 |
| | $A_{0.1‰}$ | 10.95 | 983 | 51328 |
| | $A_{0.2‰}$ | 11.70 | 1045 | 91699 |
| QS-2 | $A_{10\%}$ | 9.18 | 480 | 21759 |
| | $A_{0.1‰}$ | 10.25 | 996 | 47995 |
| | $A_{0.2‰}$ | 10.45 | 1030 | 63489 |
| QS-3 | $A_{10\%}$ | 10.95 | 475 | 33396 |
| | $A_{0.1‰}$ | 13.02 | 1249 | 87662 |
| | $A_{0.2‰}$ | 13.43 | 1349 | 120439 |
| QS-4 | $A_{10\%}$ | 7.28 | 357 | 23853 |
| | $A_{0.1‰}$ | 7.05 | 733 | 28972 |
| | $A_{0.2‰}$ | 6.92 | 1182 | 37947 |

significant decrease of the deformation modulus is noticeable because matrix discontinuities start to form. The stress at point $A_0$ is thus taken as the matrix tensile strength. As discussed in section 5.3, the lowest values of fiber orientation $\mu_{0,y}$ and parameter $\lambda = r_{Ut} V_f \frac{l_f}{d_f}$ are all on the casting surface for each specimen. Thus, the matrix discontinuity would appear first on the casting surface at point $A_0$.

For specimens QS-1 to 4, only the casting surface of specimen QS-2 is monitored and analyzed by the DIC technique. Accordingly, at point $A_0$ few short matrix discontinuities are found only on the DIC strain contour of specimen QS-2 (Fig. 18 a)). Nevertheless, as shown in Fig. 17 b) to 20 b), a small peak of instant AE events around point $A_0$ has been detected for all specimens, which indicates that matrix discontinuities develop from point $A_0$ for all specimens, although some are not found on the DIC strain contour. Thus, it is appropriate to define the stress level of point $A_0$ as the matrix tensile strength of UHPFRC.

### 6.3. Elastic limit

As shown in Figs. 17 b)–20 b), for specimens QS-1 to 4, the instant AE events slightly increase until point $A_{10\%}$ and then start to increase quickly with more than 500 events until the stress levels of about 9.73 MPa, 8.07 MPa, 7.66 MPa and 5.89 MPa in the softening domain respectively.

For specimens QS-1 to 3 with hardening behavior, the cumulative AE events are 18781, 21759 and 33396 at points $A_{10\%}$. These AE events increase by more than one time to 51328, 47995 and 87662 at points $A_{0.1‰}$, and by about two times to 91699, 63489 and 120439 at points $A_{0.2‰}$. For specimen QS-4 with softening behavior, the cumulative AE events also largely increase from points $A_{10\%}$ to $A_{0.1‰}$ and $A_{0.2‰}$, i.e., from 23853 to 28972 and 37947.

As shown in Figs. 17 a)–19 a), accordingly found in the DIC strain contour of specimens QS-1 to 3, there are only several short matrix discontinuities at points $A_{10\%}$. At points $A_{0.1‰}$ and $A_{0.2‰}$, matrix
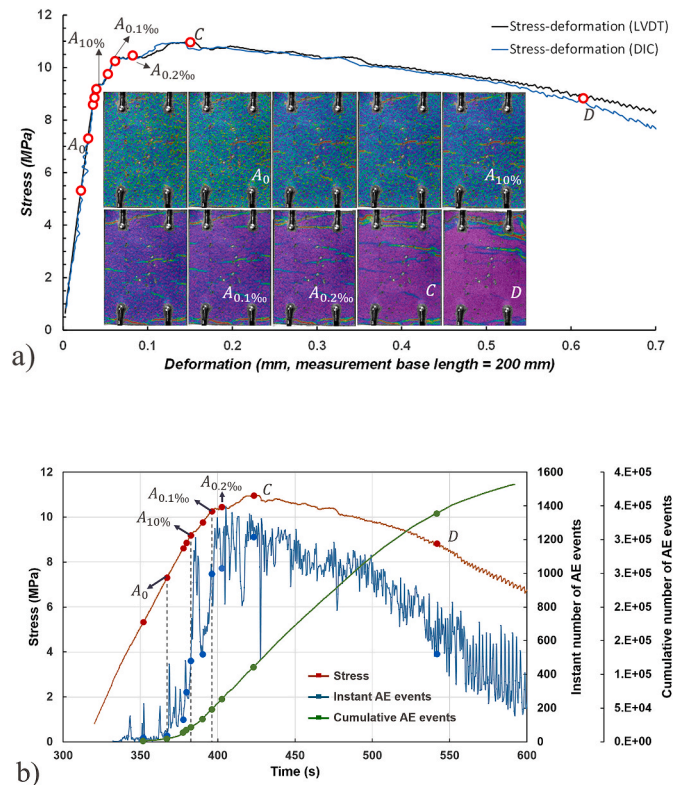


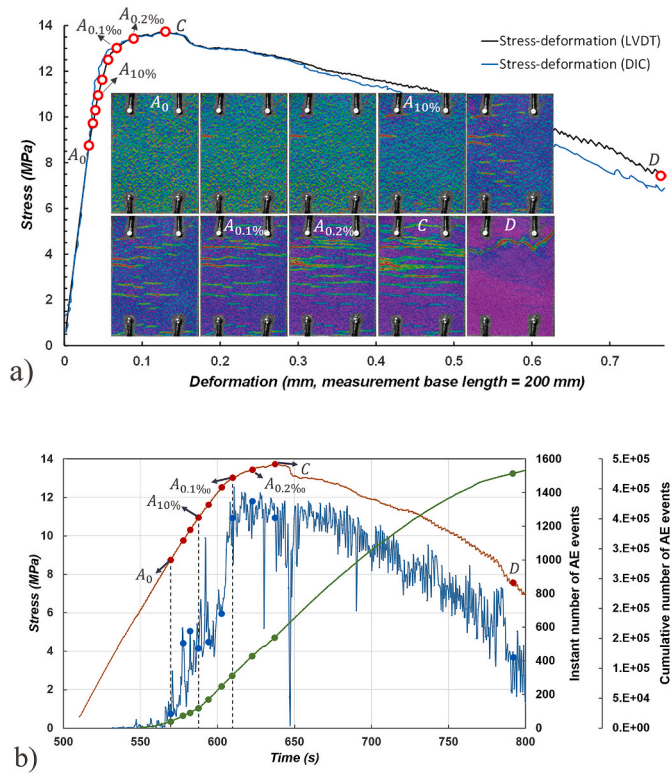**Fig. 18.** Experimental characterization of QS-2: a) DIC analysis of casting surface; b) AE analysis.

**Fig. 19.** Experimental characterization of QS-3: a) DIC analysis of sheathed surface; b) AE analysis.



**Fig. 20.** Experimental characterization of QS-4: a) DIC analysis of sheathed surface; b) AE analysis.



**Fig. 21.** Experimental characterization of QS-5: DIC analysis of sheathed surface, AE technique not used.

discontinuities significantly develop in number and length, in which at least two matrix discontinuities are longer than half of the specimen width, showing that the specimens are no longer elastic.

As shown in Fig. 20 a), on the stress-deformation curve, points $A_{0.1‰}$ and $A_{0.2‰}$ of specimens QS-4 both lie beyond the maximum tensile strength. For the DIC strain contour, there are two matrix discontinuities at point $A_{10\%}$, in which the top one percolates the specimen width and the bottom one is short. At point $A_{0.1‰}$, no new matrix discontinuity appears and the existing two discontinuities are not found to propagate. At point $A_{0.2‰}$, the bottom discontinuity develops into the fictitious crack and finally leads to specimen failure.

As discussed in section 4.2, the two strain-offset methods significantly overestimate the elastic limit of UHPFRC and the average ratios of $f_{Ute,0.1‰}$ and $f_{Ute,0.2‰}$ to $f_{Utu}$ are 0.94 and 0.96 respectively. Here, the DIC and AE results further validate this conclusion.

Besides, as obtained from the LVDT, DIC and AE results, the modulus-drop method always provides coherent results, which appropriately distinguish the elastic behavior from the hardening or softening behavior of UHPFRC. This indicates that the modulus-drop method yields the most representative value of the elastic limit among the three investigated methods.

Therefore, the elastic limit of UHPFRC may be defined as follows. The elastic limit distinguishes between the elastic behavior and the hardening or softening behavior of UHPFRC. Prior to the elastic limit, the UHPFRC tensile specimen is elastic including some minor local formation of matrix discontinuities. Beyond the elastic limit, matrix discontinuities develop quickly in number and length leading to a significant loss of specimen stiffness, while the stress is still increasing, i.e., characteristic for tensile strain hardening behavior.

## 7. Conclusions

Based on the refined characterization of five uniaxial tensile tests using four non-destructive testing methods, this paper discusses the
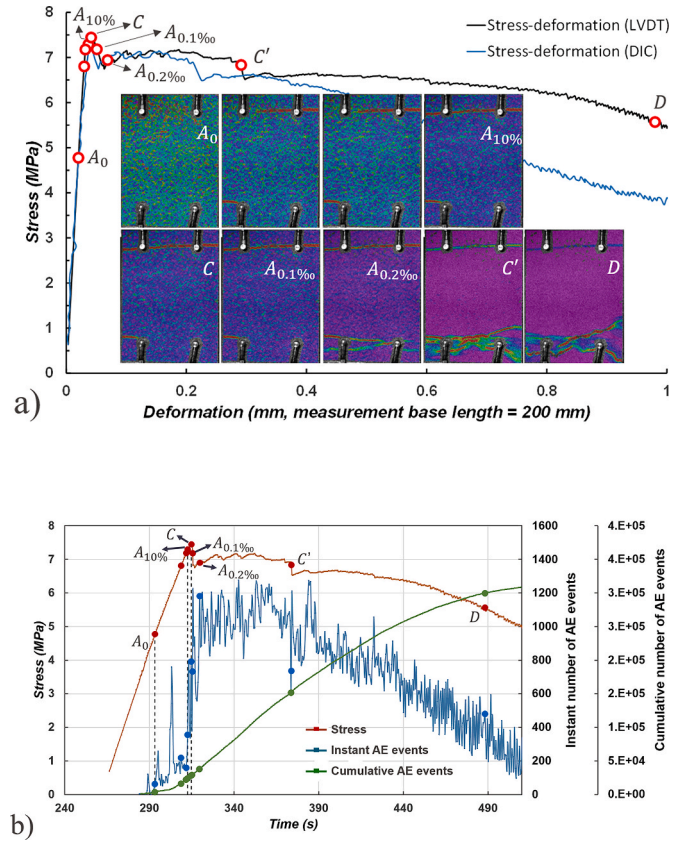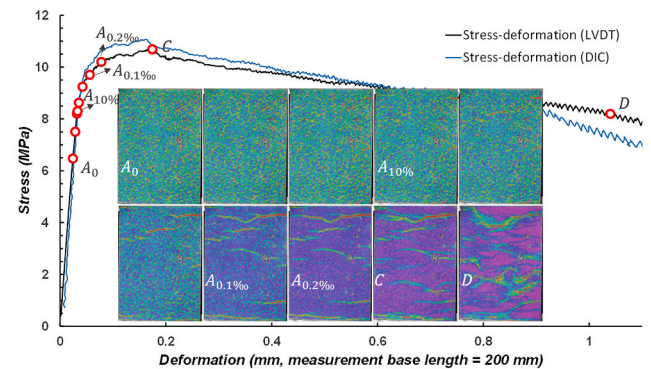
influence of fiber orientation on the elastic limit and compares three methods to determine the elastic limit tensile stress of UHPFRC. The following conclusions are reached.

(1) The elastic limit of UHPFRC is governed by contributions of the matrix and the fibrous skeleton. Analysis of experimental data from three different literature sources shows that the fiber orientation has a significant influence on the matrix tensile strength.

(2) An original model to determine the elastic limit as a function of fiber orientation is proposed and validated based on own experimental data and literature. Based on the measured local fiber distribution, this elastic limit model explains well the variation of matrix tensile strength and elastic limit of the tested specimens.

(3) This paper suggests the deformation modulus-drop method with supplementary information as a means to determine the elastic limit of UHPFRC. The detailed characterization shows that strain-offset methods overestimate the elastic limit, while the modulus-drop method always yields coherent results, allowing to distinguish between the elastic behavior and the hardening or softening behavior of UHPFRC.

(4) Using the modulus-drop method, the elastic limit is objectively and reliably determined based on rational analysis of experimental results in terms of stress and strain. The corresponding physical phenomena may be taken to define the elastic limit tensile stress of UHPFRC.

**Declaration of competing interest**

The authors declare that they have no known competing financial

interests or personal relationships that could have appeared to influence the work reported in this paper.

**Data availability**

Data will be made available on request.

**Appendix A**

Using the same UHPFRC material, fabrication and test methods as specimens QS-1 to 5, nine specimens (QS-6 to 14) are further tested. Specimens QS-7 and QS-9 are loaded until the strain of 1.2‰ and 0.7‰, while the rest of specimens are loaded until the strain of 1.5‰. After reaching the target strain, every specimen is unloaded for further use.

Regarding specimens QS-6 to 14, the local fiber volume $V_f$, local fiber orientation $\mu_{0,y}$ and local fiber distribution parameter $r_{Ut} V_f \frac{l_f}{d_f}$ are shown in Figs. 22–24, respectively. The stress-strain curves are shown in Figs. 25 and 26. The fiber orientation and elastic limit from model and test results are shown in Fig. 27 and Table 9. These results further validate that the elastic limit of UHPFRC can be appropriately estimated using the proposed relation model.
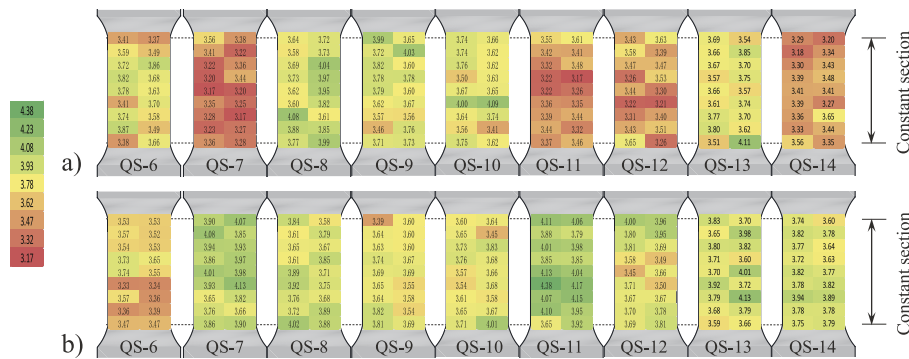


**Fig. 22.** Local fiber volume $V_f$ for specimens QS-6 to 14: a) casting surface; b) sheathed surface (unit: %).
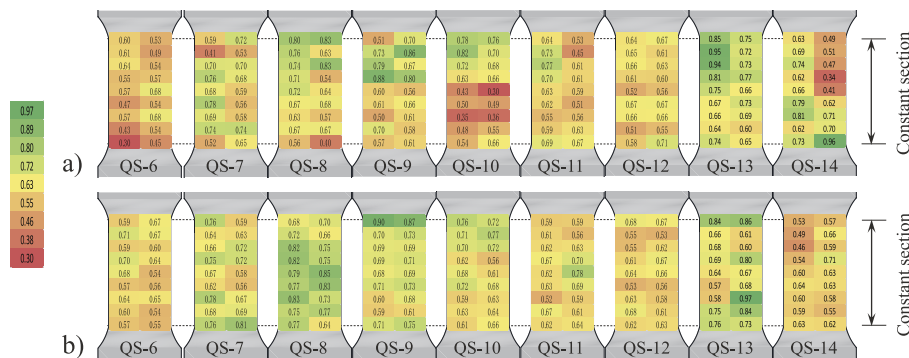


**Fig. 23.** Local fiber orientation $\mu_{0,y}$ for specimens QS-6 to 14: a) casting surface; b) sheathed surface. .
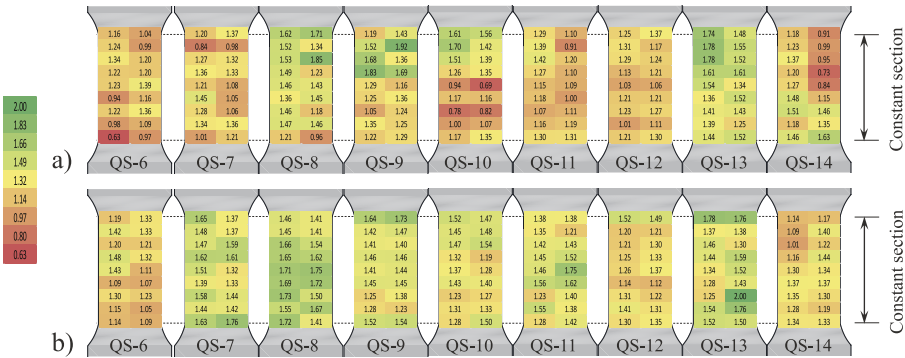
**Fig. 24.** Local fiber distribution parameter $r_{Ut} V_f \frac{l_f}{d_f}$ for specimens QS-6 to 14: a) casting surface; b) sheathed surface. .
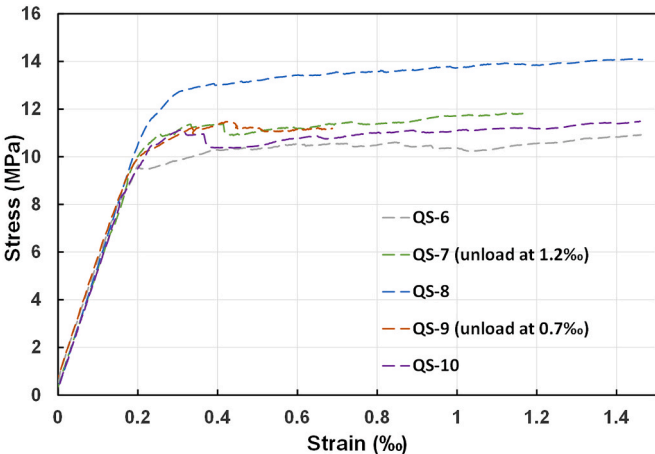


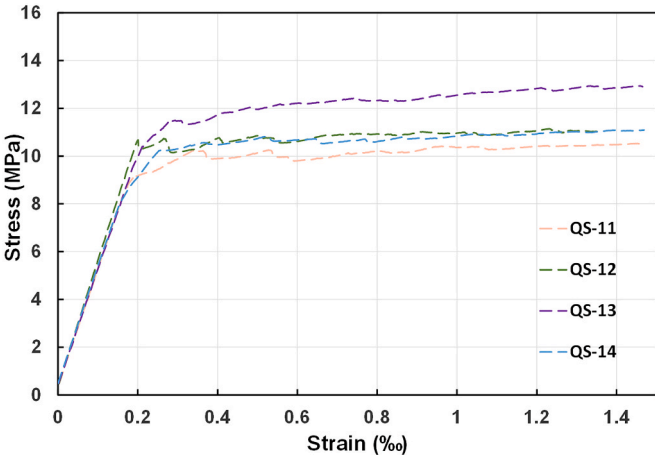**Fig. 25.** Stress-strain curves of specimens QS-6 to 10. .



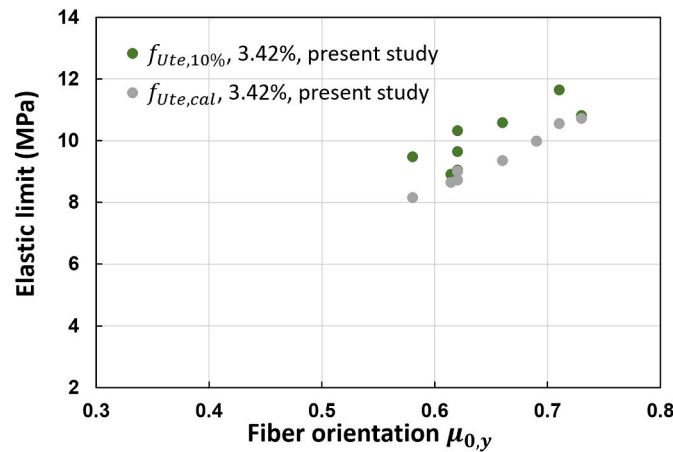**Fig. 26.** Stress-strain curves of specimens QS-11 to 14. .

**Fig. 27.** Fiber orientation and elastic limit from model and test results for specimens QS-6 to 14. .

**Table 9**
Tensile properties of specimens QS-6 to 14

| Specimen | $V_f \frac{l_f}{d_f}$ | $\mu_{0,y}$ | $\mu_1$ | $\tau_f$ (MPa) | $r_{Ut}$ | $f_{max}$ (MPa) | $f_{Ute,10\%}$ (MPa) | $f_{Ute,cal}$ (MPa) | $\varepsilon_{Ute,10\%}$ (‰) | $\varepsilon_{max}$ (‰) |
|---|---|---|---|---|---|---|---|---|---|---|
| QS-6 | 2.89 | 0.58 | 0.93 | 7.0** | 0.41 | 10.88 | 9.49 | 8.27 | 0.20 | 1.5 |
| QS-7 | 2.93 | 0.66 | 0.97 | | 0.46 | 11.84 | 10.59 | 9.39 | 0.23 | 1.5 |
| QS-8 | 3.07 | 0.71 | 0.99 | | 0.49 | 13.90 | 11.66 | 10.54 | 0.25 | 1.5 |
| QS-9 | 2.99 | 0.69 | 0.98 | | 0.48 | 11.48 | 10.00 | 10.00 | 0.20 | 0.70 |
| QS-10 | 2.99 | 0.62 | 0.95 | | 0.43 | 11.51 | 9.66 | 9.08 | 0.21 | 1.5 |
| QS-11 | 3.00 | 0.62 | 0.95 | | 0.43 | 10.39 | 9.05 | 9.10 | 0.20 | 1.5 |
| QS-12 | 2.90 | 0.62 | 0.95 | | 0.43 | 11.15* | 10.33 | 8.80 | 0.21 | 1.23* |
| QS-13 | 3.04 | 0.73 | 1.00 | | 0.50 | 12.95 | 10.83 | 10.69 | 0.24 | 1.5 |
| QS-14 | 2.90 | 0.61 | 0.95 | | 0.43 | 11.09 | 8.92 | 8.73 | 0.19 | 1.5 |

$f_{max}$ and $\varepsilon_{max}$ refers to the maximum tensile stress reached during the loading and the corresponding strain. *: The tensile strength is reached during loading. **: Specimens T1 to 5 [4] and QS-1 to 5 respectively use the similar and same UHPFRC materials as specimens QS-6 to 14. Because the tensile strength is not obtained to calculate $\tau_f$ for specimens QS-6 to 14 (except QS-12), the average $\tau_f$ of 7 MPa is taken based on $\tau_f$ of specimens T1 to 5 [4] and QS-1 to 5 shown in Table 7.

## References

[1] E. Brühwiler, UHPFRC technology to enhance the performance of existing concrete bridges, Struct. Infrastruct. Eng. 16 (2020) 94–105, https://doi.org/10.1080/15732479.2019.1605395.

[2] C. Shi, Z. Wu, J. Xiao, D. Wang, Z. Huang, Z. Fang, A review on ultra high performance concrete: Part I. Raw materials and mixture design, Construct. Build. Mater. 101 (2015) 741–751, https://doi.org/10.1016/j.conbuildmat.2015.10.088.

[3] J. Yang, R. Chen, Z. Zhang, Y. Zou, J. Zhou, J. Xia, Experimental study on the ultimate bearing capacity of damaged RC arches strengthened with ultra-high performance concrete, Eng. Struct. 279 (2023), 115611, https://doi.org/10.1016/j.engstruct.2023.115611.

[4] X. Shen, E. Brühwiler, Influence of local fiber distribution on tensile behavior of strain hardening UHPFRC using NDT and DIC, Cement Concr. Res. 132 (2020), 106042, https://doi.org/10.1016/j.cemconres.2020.106042.

[5] K. Wille, S. El-Tawil, A.E. Naaman, Properties of strain hardening ultra high performance fiber reinforced concrete (UHP-FRC) under direct tensile loading, Cem. Concr. Compos. 48 (2014) 53–66, https://doi.org/10.1016/j.cemconcomp.2013.12.015.

[6] A.E. Naaman, High performance fiber reinforced cement composites, Naaman AE High-Perform. Constr. Mater. Sci. Appl. Singap. World Sci. Publ. (2008) 91–153.

[7] NFP 18-470. https://infostore.saiglobal.com/en-us/Standards/NFP-18-470-2016-79837_SAIG_AFNOR_AFNOR_168354/, 2016. (Accessed 5 February 2022).

[8] T. Makita, E. Brühwiler, Tensile fatigue behaviour of ultra-high performance fibre reinforced concrete (UHPFRC), Mater. Struct. 47 (2014) 475–491, https://doi.org/10.1617/s11527-013-0073-x.

[9] SIA Technical Leaflet 2052, Ultra-high Performance Fibre Reinforced Cement-Based Composites (UHPFRC): Construction Material, Dimensioning and Application, 2016. http://infoscience.epfl.ch/record/225460.

[10] P. Tjiptobroto, Tensile Strain Hardening of High-Performance Fiber-Reinforced Cement-Based Composites, Doctoral thesis, University of Michigan, 1991.

[11] P. Tjiptobroto, W. Hansen, Model for predicting the elastic strain of FRC containing high volume fractions of discontinuous fibers, Mater. J. 90 (1993) 134–142, https://doi.org/10.14359/4007.

[12] S. Delsol, J.-P. Charron, Numerical modelling of UHPFRC mechanical behavior based on fibre orientation, in: Symp. Ultra-high Perform. Fibre-Reinf. Concr., 2013, pp. 679–688. Marseille, France.

[13] L.F. Maya Duque, B. Graybeal, Fiber orientation distribution and tensile mechanical response in UHPFRC, Mater. Struct. 50 (2017) 55, https://doi.org/10.1617/s11527-016-0914-5.

[14] C. Oesterlee, Structural Response of Reinforced UHPFRC and RC Composite Members, Ecole Polytechnique Fédérale de Lausanne (EPFL), 2010, https://doi.org/10.5075/epfl-thesis-4848.

[15] S. Nunes, M. Pimentel, F. Ribeiro, P. Milheiro-Oliveira, A. Carvalho, Estimation of the tensile strength of UHPFRC layers based on non-destructive assessment of the fibre content and orientation, Cem. Concr. Compos. 83 (2017) 222–238.

[16] R.G. El-Helou, Z.B. Haber, B.A. Graybeal, Mechanical behavior and design properties of ultra-high- performance concrete (open source), Mater. J. 119 (2022) 181–194, https://doi.org/10.14359/51734194.

[17] J.-Y. Wang, J.-Y. Guo, Damage investigation of ultra high performance concrete under direct tensile test using acoustic emission techniques, Cem. Concr. Compos. 88 (2018) 17–28, https://doi.org/10.1016/j.cemconcomp.2018.01.007.

[18] B.A. Graybeal, Tensile mechanical response of ultra-high-performance concrete, Adv. Civ. Eng. Mater. 4 (2015). https://trid.trb.org/view/1421504. (Accessed 22 May 2022).

[19] B.A. Graybeal, F. Baby, Development of direct tension test method for ultra-high-performance fiber-reinforced concrete, ACI Mater. J. 110 (2013) 177–186.

[20] Z.T. Bieniawski, Determining rock mass deformability: experience from case histories, Int. J. Rock Mech. Min. Sci. Geomech. Abstr. 15 (1978) 237–247, https://doi.org/10.1016/0148-9062(78)90956-7.

[21] E. Denarié, Essais de caractérisation – réponse en traction, 978-2-940156-50-4 et Berner Fachhochschule ISBN 978-3-9523787-6-2, in: E. Brühwiler, C. Oesterlee, D. Redaelli, R. Suter (Eds.), Actes de la 2ème Journée d'étude du 22 octobre 2015: Béton Fibré Ultra-Performant – concevoir, dimensionner, construire, Haute école d'ingénierie et d'architecture Fribourg, 2015, pp. 25–36 (in French), https://infoscience.epfl.ch/record/299920?&ln=en.

[22] Characterization of the tensile response of strain hardening UHPFRC - chillon viaducts, in: E. Denarié, L. Sofia, E. Brühwiler (Eds.), Proc. AFGC-ACI-Fib-RILEM Int Symp. Ultra-High Perform. Fibre-Reinf. Concr. UHPFRC 2017 106 (2017).

[23] E. Denarié, Recommendations for the Improvement of Annexes D and E of SIA CT 2052, 2016. Private Communication to Prof. Dr. Cornelius Oesterlee (Bern University of Applied Sciences, Also Chair of SIA CT 2052 Committee), Email from E. Denarié from 6.12.2016.

[24] A.E. Naaman, A Statistical Theory of Strength for Fiber Reinforced Concrete, Doctoral thesis, Massachusetts Institute of Technology, 1972.

[25] A.E. Naaman, Fiber Reinforced Cement and Concrete Composites, Techno press 3000, Sarasota, FL, USA, 2018.

[26] A. Hillerborg, Analysis of one single crack, in: F.H. Wittmann (Ed.), Fract. Mech. Concr. Dev. Civ. Eng., Elsevier, 1983, pp. 223–249.

[27] J. López, P. Serna, J. Navarro-Gregori, H. Coll, Characterisation of the strain-hardening behaviour of UHPRC using the Third-Point-Bending Test, in: Proc. 4th HIPERMAT Int. Symp, . UHPC Kassel Ger., 2016.

[28] J. Martínez, Characterisation of the Tensile Behaviour of UHPFRC by Means of Four-point Bending Tests, Doctoral Thesis, Universitat Politècnica de València, 2017.

[29] P.J. Hannant, Fiber Cements and Fiber Conretes, Mineralogical Society, England, 1978. https://trid.trb.org/view/87018. (Accessed 21 November 2021).

[30] M. Bastien-Masse, E. Denarié, E. Brühwiler, Effect of fiber orientation on the in-plane tensile response of UHPFRC reinforcement layers, Cem. Concr. Compos. 67 (2016) 111–125.

[31] P. Soroushian, C.-D. Lee, Distribution and orientation of fibers in steel fiber reinforced concrete, Mater. J. 87 (1990) 433–439.

[32] P. Stroeven, Stereological principles of spatial modeling applied to steel fiber-reinforced concrete in tension, ACI Mater. J. 106 (2009) 213.

[33] K. Wille, N.V. Tue, G.J. Parra-Montesinos, Fiber distribution and orientation in UHP-FRC beams and their effect on backward analysis, Mater. Struct. 47 (2014) 1825–1838, https://doi.org/10.1617/s11527-013-0153-y.

[34] J. Jungwirth, Zum Tragverhalten von zugbeanspruchten Bauteilen aus Ultra-Hochleistungs-Faserbeton, EPFL, 2006, https://doi.org/10.5075/epfl-thesis-3429.

[35] R.N. Swamy, P.S. Mangat, A theory for the flexural strength of steel fiber reinforced concrete, Cement Concr. Res. 4 (1974) 313–325.

[36] A. Bentur, S. Mindess, Fibre Reinforced Cementitious Composites, Crc Press, 2006.

[37] F. Laranjeira, A. Aguado, C. Molins, S. Grünewald, J. Walraven, S. Cavalaro, Framework to predict the orientation of fibers in FRC: a novel philosophy, Cem. Concr. Res. 42 (2012) 752–768, https://doi.org/10.1016/j.cemconres.2012.02.013.

[38] J. Wuest, Comportement structural des bétons de fibres ultra performants en traction dans des éléments composés, Infoscience, 2007, https://doi.org/10.5075/epfl-thesis-3987.

[39] J. Wuest, E. Brühwiler, Model for predicting the UHPFRC tensile hardening, in: Ultra High Perform. Concr. UHPC Proc. Second Int. Symp. Ultra High Perform. Concr., Kassel, Germany, 2008, p. 153.

[40] L. Martinie, N. Roussel, Simple tools for fiber orientation prediction in industrial practice, Cement Concr. Res. 41 (2011) 993–1000, https://doi.org/10.1016/j.cemconres.2011.05.008.

[41] T.L. Anderson, Fracture Mechanics: Fundamentals and Applications, CRC press, 2017.

[42] C.E. Inglis, Stresses in a plate due to the presence of cracks and sharp corners, Trans Inst Nav. Arch. 55 (1913) 219–241.

[43] ASTM C1856/C1856M-17, Standard Practice for Fabricating and Testing Specimens of Ultra-high Performance Concrete, 2017, https://doi.org/10.1520/C1856_C1856M-17.

[44] ASTM C230/C230M-14, Standard specification for flow table for use in tests of hydraulic cement. https://standards.globalspec.com/std/3855667/ASTM%20C230/C230M-14, 2020. (Accessed 24 April 2022).

[45] ASTM C1437-15, Standard test method for flow of hydraulic cement mortar. https://webstore.ansi.org/Standards/ASTM/astmc143715, 2015. (Accessed 14 October 2022).

[46] H. Neuber, Der zugbeanspruchte Flachstab mit optimalem Querschnittsübergang, Forsch. Im Ingenieurwesen. 35 (1969) 29–30, https://doi.org/10.1007/BF02559032.

[47] K. Habel, M. Viviani, E. Denarié, E. Brühwiler, Development of the mechanical properties of an ultra-high performance fiber reinforced concrete (UHPFRC), Cement Concr. Res. 36 (2006) 1362–1370, https://doi.org/10.1016/j.cemconres.2006.03.009.

[48] A. Helbling, E. Brühwiler, Eine neue Halterung für Zugversuche mit Beton-Probekörper, Mater. Technol. 4 (1987) 103–107.

[49] NF EN 1330-9, 2017. https://www.boutique.afnor.org/en-gb/standard/nf-en-13309/nondestructive-testing-terminology-part-9-terms-used-in-acoustic-emission-t/fa148827/33631. (Accessed 18 April 2022).

[50] S. Nunes, M. Pimentel, A. Carvalho, Non-destructive assessment of fibre content and orientation in UHPFRC layers based on a magnetic method, Cem. Concr. Compos. 72 (2016) 66–79, https://doi.org/10.1016/j.cemconcomp.2016.05.024.

[51] B. Sawicki, E. Brühwiler, E. Denarié, Inverse analysis of R-UHPFRC beams to determine the flexural response under service loading and at ultimate resistance, J. Struct. Eng. 148 (2022), 04021260, https://doi.org/10.1061/(ASCE)ST.1943–541X.0003239.

[52] L. Li, J. Xia, I. Galobardes, Magnetic probe to test spatial distribution of steel fibres in UHPFRC prisms, in: Proc. 5th Int. Fib Congr. Better-Smarter-Stronger Melb. Aust., 2018, pp. 7–11.

[53] M.A. Hafiz, E. Denarié, Tensile response of UHPFRC under very low strain rates and low temperatures, Cement Concr. Res. 133 (2020), 106067, https://doi.org/10.1016/j.cemconres.2020.106067.

[54] E. Absi, Bétons de fibres - Synthèse des études et recherches réalisées au CEBTP, Ann. Inst. Tech. Batiment Trav. Publics, 1994. https://trid.trb.org/view/1003606. (Accessed 23 March 2022).

[55] L. Ferrara, N. Ozyurt, M. di Prisco, High mechanical performance of fibre reinforced cementitious composites: the role of "casting-flow induced" fibre orientation, Mater. Struct. 44 (2011) 109–128, https://doi.org/10.1617/s11527-010-9613-9.

[56] I. Bayane, E. Brühwiler, Structural condition assessment of reinforced-concrete bridges based on acoustic emission and strain measurements, J. Civ. Struct. Health Monit. 10 (2020) 1037–1055, https://doi.org/10.1007/s13349-020-00433-0.

[57] C. Grosse, M. Ohtsu (Eds.), Acoustic Emission Testing, Springer Berlin Heidelberg, Berlin, Heidelberg, 2008, https://doi.org/10.1007/978-3-540-69972-9.

[58] C. Bian, J.-Y. Wang, J.-Y. Guo, Damage mechanism of ultra-high performance fibre reinforced concrete at different stages of direct tensile test based on acoustic emission analysis, Construct. Build. Mater. 267 (2021), 120927, https://doi.org/10.1016/j.conbuildmat.2020.120927.

[59] J.-Y. Wang, Z.-Z. Chen, K. Wu, Properties of calcium sulfoaluminate cement made ultra-high performance concrete: tensile performance, acoustic emission monitoring of damage evolution and microstructure, Construct. Build. Mater. 208 (2019) 767–779, https://doi.org/10.1016/j.conbuildmat.2019.03.057.